universität wien

MASTERARBEIT / MASTER'S THESIS

Titel der Masterarbeit / Title of the Master's Thesis

„Measuring the interlayer distance of twisted bilayer graphene using interferometric 4D-STEM“

verfasst von / submitted by

Clara Kofler, BSc

angestrebter akademischer Grad / in partial fulfilment of the requirements for the degree of

Master of Science (MSc)

Wien, 2023 / Vienna, 2023

Studienkennzahl lt. Studienblatt / degree programme code as it appears on the student record sheet:	A 066 876
Studienrichtung lt. Studienblatt / degree programme as it appears on the student record sheet:	Masterstudium Physik
Betreut von / Supervisor:	Univ.-Prof. Dr. Jani Kotakoski

Abstract

In this work the method of defocused four-dimensional scanning transmission electron microscopy (4D-STEM) is developed and used at the Nion UltraSTEM 100 in Vienna with the goal of measuring the interlayer distance of twisted bilayer graphene (tBLG) depending on the position in the moiré pattern inherent to these structures. The interference features formed by the overlap of diffraction disks originating from the two layers were analysed using self-written code to calculate values of interlayer distance and defocus. The test of the analysis method on a simulated dataset showed good agreement of the average interlayer distance and defocus with expectations, however the expected structure dependence could not be reproduced. For experimental measurements tBLG samples were produced by transfer of chemical vapour deposition (CVD) grown graphene monolayers onto SiN transmission electron microscopy (TEM) grids and subsequent folding by heat treatment with a laser under ultra high vacuum (UHV) conditions. The average interlayer distance value found experimentally was significantly higher than density functional theory (DFT) calculations suggest for similar structures and the interlayer distance variation could not be related to the moiré pattern. The method is promising, but more work is needed before meaningful results can be reliably obtained.

Kurzfassung

Das Ziel dieser Arbeit war es, die Methode der defokusierten vierdimensionalen Rastertransmissionselektronenmikroskopie am Nion UltraSTEM 100 der Universität Wien zu entwickeln und zu verwenden um die Distanz der Atomlagen von verdrehtem zweilagigem Graphen abhängig von der Position in ihrer Moiré Superstruktur zu messen. Die Interferenzmuster, welche durch die Überlagerung der Streuungsbilder der beiden Lagen entstehen, wurden mit selbst geschriebenem Code analysiert um Werte für die Distanz der Lagen und den Defocus zu berechnen. Der Test der Methode an einem simulierten Datenset zeigte eine gute Übereinstimmung der mittleren Distanz der Atomlagen und des Defocus' mit den Erwartungen, jedoch konnte die Strukturabhängigkeit nicht korrekt reproduziert werden. Zur Herstellung von zweilagigen Graphen Proben für experimentelle Messungen wurde einlagiges, durch chemische Gasphasenabscheidung gewachsenes Graphen auf SiN Transmissionselektronenmikroskopie Gitter transferiert und durch Bestrahlung mit einem Laser erhitzt um Falten von zweilagigem Graphen zu erzeugen. Der experimentell bestimmte mittlere Wert für die Distanz der Lagen war signifikant größer als Dichtefunktionaltheorie Berechnungen ähnlicher Strukturen zu erwarten geben und auch die Variation der Distanz der Lagen konnte nicht mit der Moiré Struktur in Zusammenhang gebracht werden. Die Methode zeigt viel Potential, jedoch gibt es immer noch Probleme mit der momentanen Arbeitsweise, welche gelöst werden müssen bevor aussagekräftige Resultate erzielt werden können.

Acknowledgements

The last few years working with and for the PNM group, starting off with producing dozens and hundreds of insufficient and worse hexagonal boron nitride samples, slowly and steadily learning my way around the lab(s) and instruments and people, finding friends on the way and finally writing my master thesis, have not always been easy, but brilliant nonetheless.

I want to start off by acknowledging just how much I have enjoyed my master studies - it is definitely ranked in the top tier of my experiences. While I am sure that everyone in my closer surroundings has helped me at one time or another, there are some people who deserve a special mention.

Let me start off with my supervisors, friends and colleagues in the PNM group.

First of all, I have to thank my supervisor Univ.-Prof. Dr. Jani Kotakoski. Of course, one is expected to thank the supervisor in this section of a thesis, but I want to make it clear, that I am not thanking Jani because it is tradition, but because he has been a great supervisor. He has been a calming presence watching out for me the whole time I have been here. Always helping when guidance, knowledge or reassurance is needed, but still leaving enough room for one to learn, and grow from the challenges that are presenting themselves. So, thank you Jani. It has been a pleasure.

The same goes for Clemens Mangler, who not just always knows the right thing to do when the microscope or laser has a bad day, calming it down or pepping it up with a large reservoir of patience and skill, but has also made the the Sternwarte lab feel like a home to me.

Next, I also want to give a special mention to my good friend and colleague Manuel Längle, whom I could always count on to give me advice personal and work related matters, moral support when I was stressed and anxious, and who was always ready to lighten the mood with fantastic situational comedy. Also a thanks to him for introducing me to Jugger, a sport that has given me a well needed second life focus, made me part of a great community and provided me with some of my closest friends.

Another special thanks goes to Toma Susi, who has offered some great advice in matters of simulations, and has always made time for me when I needed his help.

Also Wael Joudi will have my eternal gratitude, without him I would still be struggling to prepare samples, and nobody would be reading this thesis right now.

The 3222 crew in general has been great company. The snide humour of Carsten, the 'great' jokes of Wael, the late night work/ice cream sessions with Barbara, the fruitful discussions with David and the generally just good times with Manuel have made my day to day life so much better.

Also a special mention to Alissa, who I have been working with a lot and who has made all struggles with the instrumentation much more bearable.

I have not had that much life outside work lately, but in the life that I do have, there are a few very special people. Most notably my family - my mother and father Sigrid and Tomi who have not only handed me the tools to be independent and self sufficient, but have supported me through everything, as well as my older sister Flora, my protector and partner in any kind of shenanigans.

Beside my family, my friends from Jugger, the Scouts and the university have done a great job in keeping me sane - or at least as sane as I was before I started studying.

A last mention goes to Thor Heyerdahl, whos raft Kon-Tiki I have used as placeholder for all my unfinished figures in the thesis, because it is absolutely great, as you can see in Fig. 1.

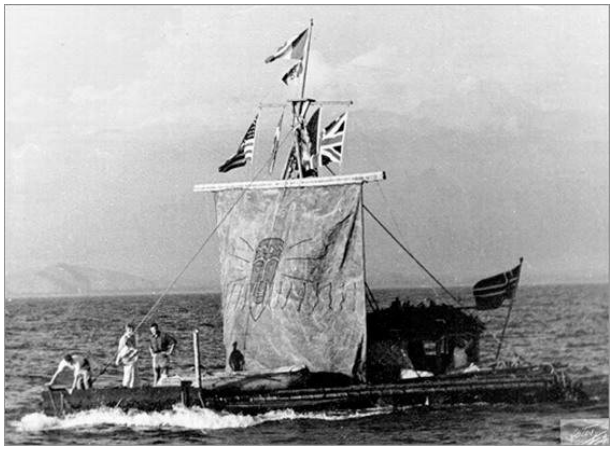

Figure 1: Kon Tiki, a raft built and used by Thor Heyerdahl in 1947 to sail almost 8000 kilometers from Peru to Polynesia and show that it could have been possible for prehistoric explorers to migrate across such distances. [1]

I could ramble on for pages and pages because I just have so many great people in my life - but this is scientific thesis about bilayer graphene and electron microscopy so I will leave it at that. Enjoy.

List of acronyms

2D two-dimensional

3D three-dimensional

4D four-dimensional

4D-STEM four-dimensional scanning transmission electron microscopy

ADF annular dark field

BF bright field

BZ Brillouin zone

CANVAS Controlled Alteration of Nanomaterials in Vacuum down to the Atomic Scale

CBED convergent beam electron diffraction

CCD charge coupled device

COM center of mass

cTEM conventional transmission electron microscopy

CVD chemical vapour deposition

DFT density functional theory

DPC differential phase contrast

FFT fast Fourier transform

HAADF high angle annular dark field

MAADF medium angle annular dark field

STEM scanning transmission electron microscopy

tBLG twisted bilayer graphene

TEM transmission electron microscopy

UHV ultra high vacuum

Contents

1 Introduction **9**

2 Materials **11**

2.1 Graphene 11

2.1.1 Structure 11

2.1.2 Properties 12

2.1.3 Synthesis of graphene 13

2.1.4 Bilayer graphene 14

3 Methods **19**

3.1 Electron microscopy 19

3.1.1 A brief history of microscopy 19

3.1.2 Transmission electron microscopy 20

3.1.3 Electron waves 20

3.1.4 Interaction cross section 21

3.1.5 Elastic scattering 22

3.1.6 Inelastic scattering 23

3.1.7 Electron diffraction 23

3.2 Instrumentation 27

3.2.1 Electron guns . . . 27
3.2.2 Electron lenses . . . 28
3.2.3 Electron detectors . . . 29
3.2.4 Aberrations and aberration correction . . . 29
3.2.5 Resolution . . . 33
3.3 Scanning transmission electron microscopy . . . 33
3.3.1 Probe formation . . . 34
3.3.2 Image formation and contrast . . . 35
3.3.3 Limitations of conventional STEM . . . 37
3.4 4D scanning transmission electron microscopy . . . 37
3.4.1 4D-STEM detectors . . . 37
3.4.2 4D-STEM imaging modes . . . 38
3.4.3 Ptychotomography . . . 40
3.5 Experimental implementation . . . 41
3.5.1 Preparation of monolayer graphene samples . . . 41
3.5.2 Sample alteration and study in the CANVAS system . . . 41
3.6 Data analysis . . . 45
3.6.1 Scaling of the images . . . 46
3.6.2 Determination of the twist angle . . . 46
3.6.3 Analysis of the defocused convergent beam electron diffraction (CBED) patterns . . . 46
3.6.4 Reconstruction of virtual images . . . 52
3.6.5 DFT calculations . . . 52
3.6.6 Image simulations . . . 52

3.6.7 Defocused 4D-STEM simulations 53

4 Results and discussion **54**

4.1 Effect of the laser for cleaning and fabrication of bilayer graphene 54

4.1.1 Cleaning effect 54

4.1.2 Creation of folds 54

4.2 Analysis of interferometric 4D-STEM data 58

4.2.1 Simulated dataset 58

4.2.2 Experimental dataset 65

4.3 Discussion 70

5 Conclusions and outlook **72**

A ... but that was not the plan! A tale of broken equipment **80**

Chapter 1

Introduction

The momentous discovery of graphene by Konstantin Novoselov and Andre Geim in 2004, a feat before presumed not to be possible because of the theorised instability of the material [2], lead to the birth of a whole new area of science dedicated to the study of two-dimensional (2D) materials and their extraordinary properties.

Tools like scanning transmission electron microscopy (STEM) provide atomic resolution images of such thin film samples, but are unfortunately at a loss when it comes to studying the three-dimensional (3D) character of these structures, that, despite their name, show some extent of buckling crucial for, e.g., the above mentioned stability of graphene [3]. Also for multilayers like bilayer graphene, the 3D structure is an interesting object of study, as a twist between the two stacked layers leads to an angle-dependent superstructure, the moiré pattern, that, e.g., for graphene has been shown in DFT calculations to have an influence on the interlayer distance [4].

One possibility to gain information on the interlayer distance of such structures that was explored by Michael Zachman et al. in 2021 [5] is defocused 4D-STEM, a method where at every sample position the whole defocused diffraction pattern is recorded. For multilayer structures these diffraction patterns consists of overlapping Bragg disks, that show interference features connected to various parameters of the scattering process, and can be used to calculate properties like the interlayer distance [5] provided large enough, clean twisted bilayer regions are available for imaging.

In this thesis, this method of 3D-resolved interferometric 4D-STEM is first implemented at the University of Vienna and tested for a simulated dataset of a DFT-relaxed twisted bilayer graphene structure from Ref. [5]. The analysis produced reasonable average values for the interlayer distance and defocus variation and showed a dependence of the interference features

on the moiré pattern. The structure dependence of the interlayer distance could, however, not be reproduced. This method was also used experimentally to find an average interlayer distance for a tBLG sample produced by heat mediated folding of a CVD grown graphene monolayer on a SiN TEM grid under UHV conditions. This sample preparation method, producing large areas of atomically clean tBLG has not been reported before.

Even though many aspects of the analysis did not go as planned and did not produce the results anticipated, this work provides a foundation upon which future experiments can be constructed.

Chapter 2

Materials

2.1 Graphene

In 2004 Konstantin Novoselov and Andre Geim managed to separate a single layer of carbon from a graphite crystal [2], in this achieving the first successful preparation of the material known as graphene. This momentous experimental breakthrough has incited intense research into 2D materials, many of which have extraordinary properties as well as interesting structures [6].

2.1.1 Structure

Graphene consists of sp^2-hybridised carbon in a planar honeycomb lattice with three valence electrons forming strong σ bonds responsible for the intralayer strength of the material and the remaining valence electron forming a π bond that governs the interlayer interaction. The structure as well as a schematic of the orbitals is shown in Fig. 2.1.

The lattice vectors are

$$\mathbf{a}_1 = \frac{a}{2}\begin{pmatrix} 1 \\ \sqrt{3} \end{pmatrix} \text{ and} \tag{2.1}$$

$$\mathbf{a}_2 = \frac{a}{2}\begin{pmatrix} 1 \\ -\sqrt{3} \end{pmatrix}, \tag{2.2}$$

where the lattice constant $a = \sqrt{3}a_{c-c} \approx 2.46$ Å can be calculated from the carbon-carbon

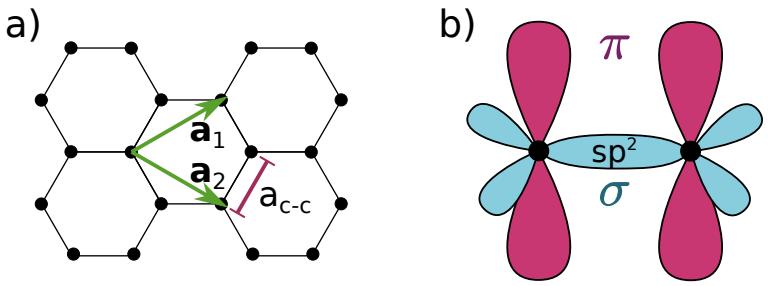

Figure 2.1: a) The structure of the graphene honeycomb lattice. Lattice vectors $\mathbf{a}_1$ and $\mathbf{a}_2$ are shown in green and the carbon-carbon distance a_{c-c} is marked in red. b) Schematic representation of the three σ orbitals per carbon atom, that form sp^2-hybridised intralayer bonds, and the perpendicular π orbitals.

distance $a_{c-c} \approx 1.42$ Å [7].

2.1.2 Properties

One main reason for the high interest in graphene is its extraordinary electronic structure. As shown in Fig. 2.2 a), the Brillouin zone (BZ) of graphene has a hexagonal symmetry just like the real space lattice and shows three high symmetry points K, K' and M. While the carbon intralayer bonds have a σ character that results in electronic bands separated by a large energy gap, the π states form a single energy band that shows a self-crossing at the K point with an energy corresponding to the Fermi-level. Because of this configuration graphene is known as a gapless semiconductor [8].

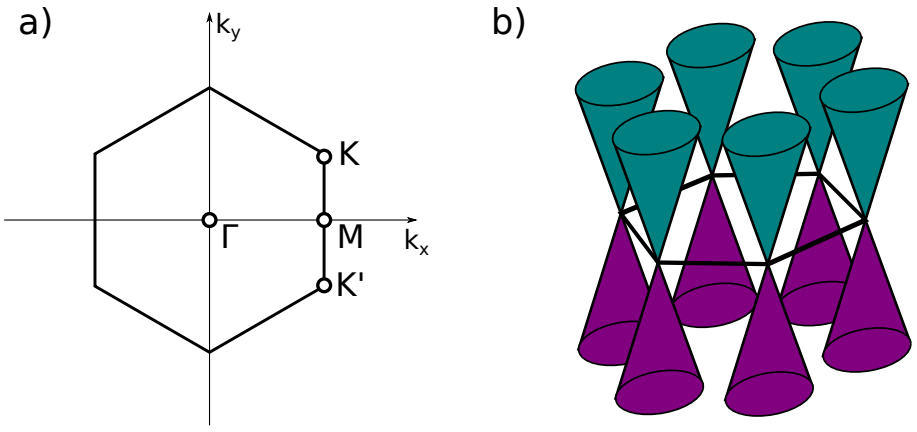

Figure 2.2: a) The hexagonal Brillouin zone of graphene with the high symmetry points K, K' and M. b) Schematic illustration of the Dirac cones with teal corresponding to the conduction and violet corresponding to the valence band.

Close to these so-called Dirac points the energy bands are linear, forming Dirac cones, and electrons behave as massless fermions leading to very high speeds of the order of 10^6 m/s [6]. The Dirac cones are illustrated in Fig. 2.2 b).

Another astounding property is the high thermal conductivity of suspended monolayer graphene. With up to approximately 5300 W/mK [9], it more than doubles the value of 2000 W/mK exhibited by graphite [6]. For this work relevant is also the negative thermal expansion coefficient of graphene – contrary to many other materials, graphene contracts when it is heated [10].

Also optically graphene shows noteworthy characteristics, like the high absorption rate of 2.3% for a monolayer, scaling linearly with number of layers [11]. Thus, even single layers of graphene can be distinguished via visible light microscopy, making mechanical exfoliation a viable tool. Notable here is, that the absorption range is not limited to a narrow spectrum, but extends over the visible and infrared region, and the absorption is determined by the fine structure constant $\alpha = e^2/\hbar = 1/137$ with an additional factor of π, and is therefore independent of the radiation frequency [11]. Further, graphene exhibits an intriguing additional degree of freedom, termed the *pseudospin*, that comes from the inequivalence of the two sublattices in the honeycomb structure and makes it very attractive for numerous potential applications [8].

The mechanical properties of graphene are also a main research focus. Many experiments and calculations have been conducted to find an accurate value for the Young's modulus, and while the exact results vary quite strongly, the studies all show extraordinarily high values in the order of 1 TPa [12], which is about five times higher than the value for stainless steel, and surpasses even synthetic diamonds that show elastic moduli of up to around 925 GPa [13].

2.1.3 Synthesis of graphene

Over the years of extensive experimental work on graphene, many different synthesis and transfer methods have emerged. While the highest quality samples are produced by exfoliating individual graphene layers from graphite, CVD allows growing larger samples with much less effort [14].

Chemical vapour deposition

Instead of starting from graphite and exfoliating single atomic layers by thinning, graphene can also be synthesised from smaller building blocks by exploiting chemical reactions.

In CVD gaseous precoursers are used to grow a film of the desired material, here graphene, on a catalytic substrate. First a mixture of carbon precursor gases (e.g., methane), carrier gases (e.g., Ar), and sometimes an activation gas (H_2), is led into the CVD tube furnace chamber where it is heated up to the point of decomposition. A graphene layer is then grown on the surface of the substrate from the decomposed molecules [14] . The graphene produced is polycystalline and has varying quality, but the yield of the method is high and the quality is sufficient for a wide range of experimental work and applications [6].

There are many variations of this process, and many all together different synthesis methods, but description of those would go beyond the scope of this thesis. For interested minds the review paper by Adrián Gutiérres-Cruz et al. from 2022 [14] is recommended.

In this thesis CVD grown graphene was used as basis to prepare bilayer samples as discussed in Sec. 3.5.

2.1.4 Bilayer graphene

When considering multiple layers of graphene, there are additional degrees of freedom for the relative atom positions and therefore infinitely many distinct crystallographic structures which can exhibit vastly different properties [7].

For bilayer graphene, the two main stacking orders are AA stacking, so the direct alignment of carbon atoms of the two layers, and the energetically more favourable AB or Bernal stacking, where each carbon atom of the second layer occupies the empty space above the centre of the first layer hexagons [15]. If the layers are twisted with respect to each other by an angle θ_t the situation becomes more complicated as moiré patterns are formed.

Moiré patterns are well known in various areas of physics and technology, and even in the fabric industry, where they were first commercially introduced in the 18th century in the form of watered silk, a french cloth that is especially woven and finished, so as to produce a wavy appearance due to interference effects [16].

Generally moiré patterns describe superstructures that emerge from the interference from two or more similar but not necessarily equal periodic structures. In condensed matter, moiré patterns are formed by stacking of atomic layers that slightly differ due to lattice mismatch, or, as in the case of twisted bilayer graphene, lattice rotation [17]. The resulting superstructures change

drastically with respect to the twist angle. While there is always some periodicity to the formed moiré patterns, for certain angles, the translational symmetry is retained and the structure is called commensurate [18].

Fig. 2.3, showcases the structure of stacked bilayer graphene with twist angles ranging between 3° and 30°.

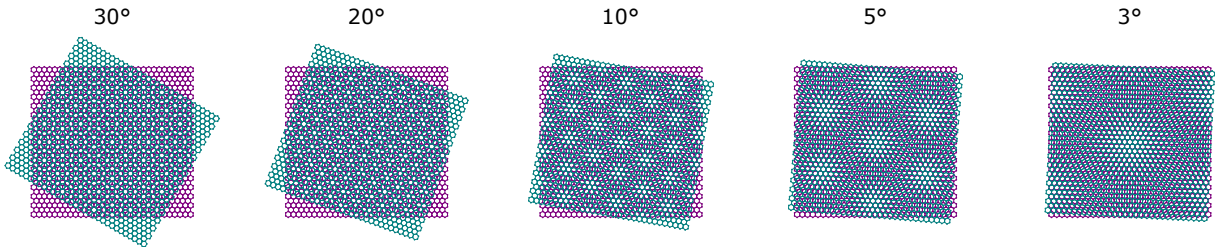

Figure 2.3: A schematic illustration of two layers of a honeycomb structure like graphene stacked and twisted with angles between 30° and 3°. The inverse relationship between twist angle and moiré cell size can be seen clearly.

It turns out, that the supercell size L_{cell} is directly connected to the twist angle θ_t through the relationship [4]

$$L_{cell} = \frac{\sqrt{3}a_{c-c}}{2\sin\theta_t/2}. \tag{2.3}$$

This formulates the inverse relationship of the twist angle and the periodicity that is already obvious from looking at the structures for different angles shown in Fig. 2.3 above. However, not only the size, but also the character of the structure changes with the twist angle. While for larger angles the structure shows little order, smaller twist angle graphene stacks have well defined areas of AA and AB stacking with transition regions in between [4].

Influence of the moiré pattern on electronic properties

The band structure is in effect just a representation of the interaction of an electron wave with a material, an interaction that is, as it turns out, not indifferent to the formation of moiré superstructures.

Uchida et al. carried out extensive DFT calculations in 2014 [4] to relate the twist angle of bilayer graphene to band structure changes and found that, while for large twist angles around 30° the two graphene layers are effectively decoupled and the band structure close to the Dirac point, as

well as the Fermi velocity, is almost unchanged from the monolayer case, smaller angles show a very different behaviour. With decreasing twist, the linear bands flatten and the Fermi velocity decreases. When the twist angle drops under 1°, the bands become basically flat over most of the BZ and the Fermi velocities therefore approach zero. Only at the Γ point a small band gap remains.

As discussed above, the BZs of monolayer graphene have a hexagonal symmetry with the Dirac cones, regions of linear dispersion, at the K and K' points where a self crossing of the bands is exhibited. With a second graphene layer in the picture, there is another, equivalent BZ that, just like the real structure, is twisted with respect to the BZ of the first layer by some angle. However, that is not all that happens. Because of the moiré pattern, there is an additional periodic superstructure, that in turn also corresponds to so-called mini-Brillouin zones formed with one hexagon side corresponding to the shift between the BZs for the two different layers as illustrated in Fig. 2.4 a).

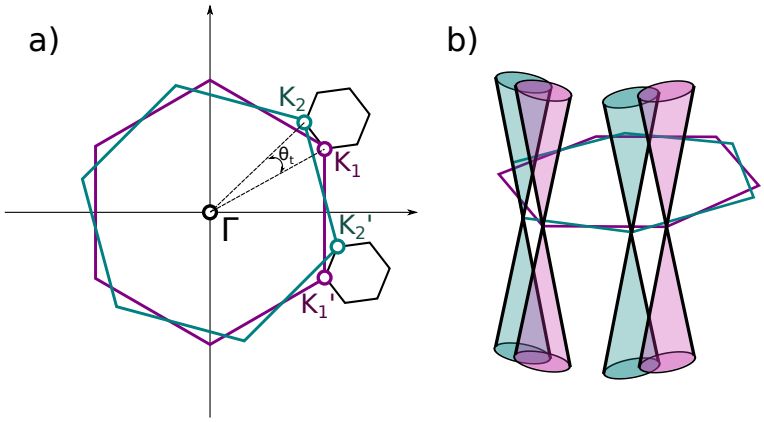

Figure 2.4: a) The Brillouin zone of twisted bilayer graphene, consisting of two twisted single layer Brillouin zones. Due to the moiré pattern, mini BZs are formed. b) The overlap of the Dirac cones shown schematically for two of the six K/K' points per layer. Based on Ref. [19].

As seen in Fig. 2.4 b), the Dirac cones of the K and K' points corresponding to the different layers overlap. With decreasing twist angle the distance of the points shrinks, the Dirac cones grow closer, and the overlap becomes more pronounced. If tunnelling between the layers is considered, it turns out, that at these Dirac cone intersections crossing is avoided, which leads to the formation of saddle points in the band structure. At these so-called van Hove singularities, a higher density of states is present. For large angles where the van Hove singularities are widely separated the effect is minimal, but with decreasing angles the coupling of the states leads to hybridisation and the van Hove peaks merge into one single peak. This is the reason for the afore

mentioned flattening of the bands [19].

Magic angles in tBLG

The flattening of the bands and consequential vanishing of the Fermi velocity is a property inherent to bilayer graphene twisted by the so-called magic angles. The largest of these occurs at around 1.1° and their exact values depend on the strength of the interlayer tunnelling as well as the nearest-neighbour electron hopping energy [19]. The non-conducting state formed at these angles is referred to as a Mott insulator and is responsible for a number of interesting properties native to these structures. The most prominent is the similar behaviour to high temperature superconductors when a few charge carriers are introduced [20].

Optical properties of twisted bilayer graphene

As was mentioned, the absorption spectrum of graphene is independent of wavelength. However for tBLG, the van Hove singularities influence the density of states, which in turn reflects on the absorption properties. For large twist angles, where the van Hove peaks are widely separated, the absorption is strongest for visible light. With decreasing twist, the absorption peak shifts towards the centre of the infrared region [20].

Fabrication and angle control

For the fabrication of tBLG, there are two possible approaches. Either the bilayers can be grown directly, or monolayer graphene can be used as a basis to tailor the desired structures.

For growing bilayers, CVD has been used successfully. However, even though the layer number and twist angle can be controlled to some extent by adjusting the composition and surface of the substrate and the parameters of the process, the properties cannot be adjusted exactly. Other downsides of the method are the variation of quality and the polycrystalline nature of the grown layer. For applications where angle control is not of the essence, the cost effectiveness and high yield of CVD growth make it a viable method [21].

For high angle control the most common methods consist of stacking or folding monolayer graphene sheets. While the naive stacking of two graphene sheets can be done easily, this will result in a bilayer sample with a random twist angle, or, if polycrystalline monolayers are

used, a bilayer with many patches of different twist angles. To have control over the angle, an alignment transfer system typically consisting of a visible light microscope and two moving sample positioning stages is used. The yield of this method is low, and the process is complicated, but the angle control makes it very useful for research purposes [21].

Another method used to produce bilayers is folding. There have been successful studies where atomic force microscopy [22] and scanning tunneling microscopy [23] setups have been used to tear and fold a graphene layer and achieve different twist angle bilayer structures. Also macroscopic folding of whole graphene layers in the sample transfer process has been reported [24]. These methods offer high variability and angle control, come however, at the cost of being complicated and introducing strain and defects in the samples [24].

In this thesis, graphene bilayers of predominantly small angles were successfully created by heat induced folding of CVD grown single layers on SiN TEM grids under UHV conditions. A detailed description of the process is given in Section 3.5.

Chapter 3

Methods

3.1 Electron microscopy

Samples were imaged using different electron microscopy techniques. In the following, electron microscopy in general will be discussed, followed by a description of STEM and 4D-STEM, the method used to acquire the data needed for the corrugation analysis.

3.1.1 A brief history of microscopy

Visible light microscopy has been used for enhancing the eyesight of humans at least since Seneca picked up a spherical flask of clear water in the first century a.d. and discovered that he could use it to magnify features in his surroundings. Over the following centuries the production of lenses was refined, and in the 16th century combinations of different lenses were first used as 'microscopes', a term branded by Giovanni Faber in 1625. With the improvement of the technology, as well as the understanding of the underlying principles resolution was optimised leading to the remarkable visible light microscopes available today. However, the possible resolution is restricted by diffraction to $d_{min} = 0.61\frac{\lambda}{NA}$, where λ is the wavelength and NA describes the numerical aperture of the lens [25]. This leads to a physical limit of about 0.2 µm [26].

The first steps towards electron imaging were taken by Prince de Broglie in 1924 with his definition of material waves, followed soon by the research on the movement of electrons in magnetic fields by H. Busch, that laid the groundwork for the design of magnetic lenses [27]. In 1937 M. von Ardenne and M. Knoll developed the first scanning electron microscope and in 1939 transmission

electron microscopes with a resolution of 7 nm were first mass produced by Siemens [28]. Even though the idea of STEM was around from the 1930s, it was not realised for a long time due to inadequate electronics, electron sources and vacuum technology [29]. Only in 1971, when Albert V. Crewe designed a STEM instrument with a field emission gun as the electron source, UHV conditions and an annular dark field detector, it was possible to produce atomic resolution images [30].

Modern TEM devices can achieve resolutions in the order of already 1 Å [31], while with STEM even sub-Ångström spacings can be resolved [32]. Even though this is impressive, there are still new developments, one of which is four 4D-STEM, where a full diffraction pattern is recorded for every pixel, leading to a four-dimensional (4D) data cube and extremely rich information for each probe position.

3.1.2 Transmission electron microscopy

TEM utilises the wave nature of electrons accelerated to high velocities and passed through a sample to reveal the structure of a thin specimen, making it possible to resolve features magnitudes smaller then possible with visible light microscopy.

There are two main types of transmission electron microscopes used for conventional transmission electron microscopy (cTEM) and STEM, their main difference being, that cTEM is a wide beam technique where a large region of the sample is irradiated by a nearly parallel electron beam, producing a 'one shot image', whereas for STEM the electron beam is focused to a sharp probe, which is scanned over the sample giving information pixel by pixel [33]. This difference is shown in Fig. 3.1.

In the following the principles that cTEM and STEM have in common will be discussed before dealing with STEM in particular in the subsequent chapters.

3.1.3 Electron waves

The wavelength λ_e of electrons accelerated to high velocities can be calculated by using de Broglie's relation

$$\lambda_e = \frac{h}{p}, \tag{3.1}$$

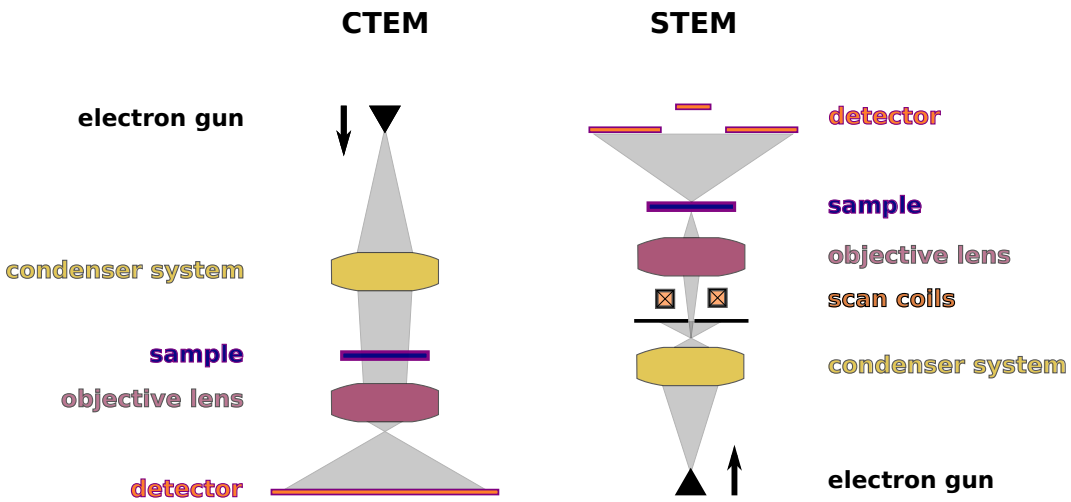

Figure 3.1: Simplified ray diagrams for cTEM and STEM. For cTEM the electron beam is parallelized before hitting the sample and the image is recorded on the screen as a one-shot image. For STEM the beam is focused to a sharp probe that is scanned over the sample and for every probe position a value is detected.

where h is Planck's constant and p is the electron momentum. If the acceleration is done via an applied potential U, the velocity of the electron can be calculated, leading to a momentum of

$$p = m_0 v = \sqrt{2 m_0 e U}, \tag{3.2}$$

with the electron (rest) mass m_0 and the elemental charge e. This equation is however only applicable for the non-relativistic case. For a more realistic description, relativistic effects have to be taken into account leading to the electron wavelength of

$$\lambda_e = \frac{h}{\sqrt{2 m_0 e U (1 + \frac{eU}{2 m_0 c^2})}}. \tag{3.3}$$

For acceleration voltages in the kV range this leads to sub-Ångström electron wavelengths [34].

3.1.4 Interaction cross section

Any signal collected in microscopy always stems from an interaction of the used probing matter (electrons in this case) with the specimen to be probed. The mathematical construct to describe an interaction is the cross section σ, which is given in units of area and, when divided by the area of the scattering centre, represents the probability of a scattering event. A concept crucial for electron microscopy is the differential cross section $\frac{\mathrm{d}\sigma}{\mathrm{d}\Omega}$, which describes the probability of the scatterers being scattered into the differential solid angle $d\Omega$ by the scattering centre [34]. A schematic illustration of the scattering process is shown in Fig. 3.2.

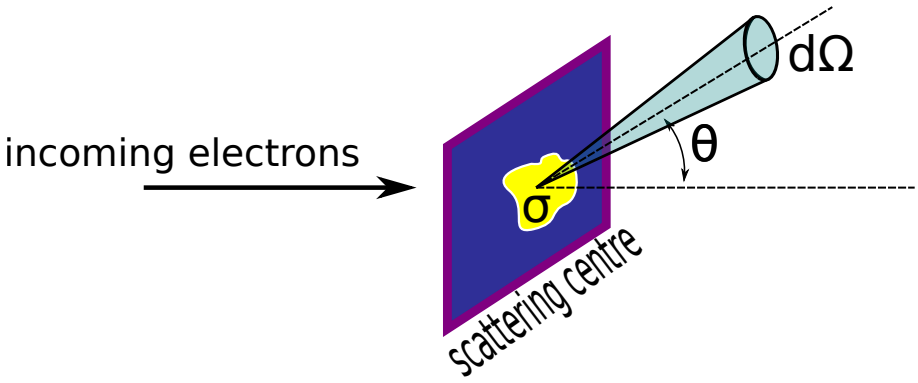

Figure 3.2: Schematic illustration of the scattering process. The differential cross section $\frac{\mathrm{d}\sigma}{\mathrm{d}\Omega}$ describes the probability of an electron being scattered into the differential solid angle $d\Omega$.

Alternatively scattering can be described using the mean free path Λ, the average distance travelled by the electrons between scattering events. Assuming N_v scattering centres per unit volume it is related to the cross section via [33]

$$\Lambda = \frac{1}{N_v \sigma}. \tag{3.4}$$

For electron microscopy the two main factors influencing the scattering cross section are the electron energy (with higher beam energy corresponding to lower cross sections), and the specimen density (with higher density leading to stronger scattering) [34].

3.1.5 Elastic scattering

Elastic scattering is characterised by the conservation of kinetic energy in the centre of mass frame and often results from an interaction of the electron with the atomic nucleus. It can be described by the differential cross section

$$\frac{\mathrm{d}\sigma}{\mathrm{d}\Omega} = \frac{4\gamma^2 Z^2}{a_0^2 q^4}, \tag{3.5}$$

where $q = 4\pi \sin(\theta/2)/\lambda$ is the scattering vector magnitude depending on the scattering angle θ and the wavelength λ. γ describes the relativistic factor, a_0 is the Bohr radius and Z is the atomic number. Elastic scattering is therefore characterised by small scattering angles θ, indicated by the proportionality of the cross section to θ^{-4} (in the approximation of small angles) [35]. This model was developed as an improvement of the Rutherford model and can be made more realistic by accounting for electron screening of the nucleus. Elastically scattered electrons are used for various diffraction techniques because of their spatially coherence [33].

3.1.6 Inelastic scattering

Inelastic scattering on the other hand describes scattering processes that lead to measurable kinetic energy losses and are often the result of interaction with the electrons surrounding the nucleus. These energy losses are used in electron energy loss spectroscopy to gain information about, e. g., the chemical composition of samples.

One example of an inelastic process is plasmon scattering, where the incident electron introduces oscillations of free electrons and dissipates significant energy (up to $\sim 30\,\mathrm{eV}$). The energy loss peaks, however, are often broad and can overlap. Also for thicker specimens there can be more then one plasmon interaction which can further complicate the analysis of the spectrum.

The most distinctive interaction is the inner shell ionisation, where inner shell electrons are excited followed by relaxation under emission of either characteristic X-rays or an Auger electron. Even though the cross section for this interaction is quite small, this is the signal most used in electron energy loss spectroscopy (EELS) because the very distinctive energy loss associated with this process gives reliable information about the atomic species and the interatomic bonding [33].

There are various other inelastic scattering processes that can be used in electron microscopy and spectroscopy that will not be discussed here.

3.1.7 Electron diffraction

Electrons passing through a specimen will be scattered, giving a diffracted wavefront with a character depending on the phase relation of the scattered electrons determined by the angle between the incoming and outgoing beams and the diffracting planes. Constructive interference will only occur if the difference of the incoming and diffracted wavevectors $\mathbf{k}_0$ and $\mathbf{k}_d$ is a reciprocal lattice vector $\mathbf{g}$,

$$\Delta\mathbf{k} = \mathbf{k}_d - \mathbf{k}_0 = \mathbf{g}. \tag{3.6}$$

This so-called Laue condition is equivalent to Bragg's law for a diffraction order n

$$2d\sin\theta = n\lambda, \tag{3.7}$$

that connects the angle between incident beam and scattering plane θ with the wavelength λ and the lattice plane spacing d. The geometry of this scattering process is schematically shown in Fig. 3.3.

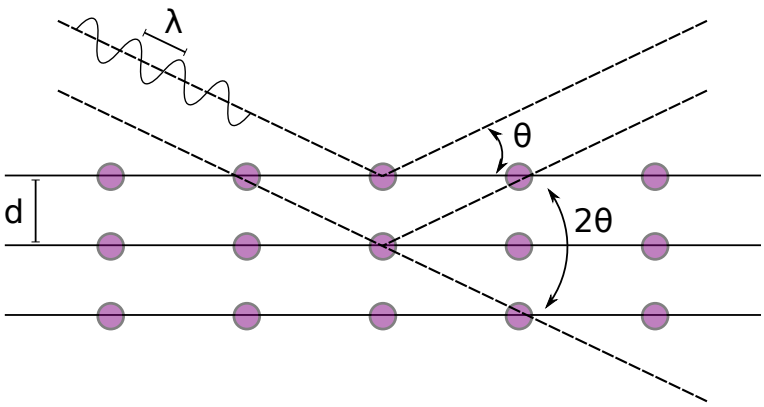

Figure 3.3: Schematic illustration of the scattering process. The incoming beam of wavelength λ is scattered at the lattice planes with spacing d at an angle θ.

A useful concept to visualize the diffraction condition in crystals is the Ewald sphere, a sphere with radius $|\mathbf{k}| = 1/\lambda$ passing through the origin of the reciprocal crystal lattice as seen in Fig. 3.4 for a 2D intersection. The Laue condition is fulfilled for every reciprocal lattice point intersecting the sphere surface. However, in thin crystals the points are broadened to reciprocal lattice rods (relrods) leading to reflections even if the Laue condition is not satisfied exactly [34].

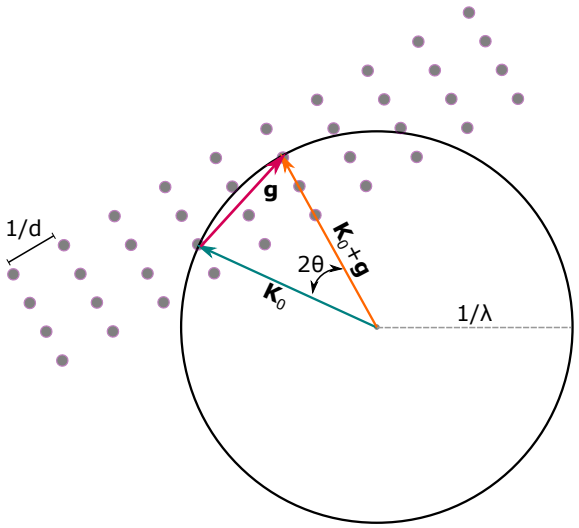

Figure 3.4: Ewald sphere construction with the diffraction angle θ, the incident and diffracted wavevectors $\mathbf{K}_0$ and $\mathbf{K}_0+\mathbf{g}$ each with length $1/\lambda$, the reciprocal lattice vector $\mathbf{g}$ and the reciprocal lattice plane distance $1/d$.

A plane of reciprocal lattice points containing the origin that is (close to) perpendicular to the incident beam is called the zero order Laue zone and contains most reflections for small diffraction angles because the reciprocal lattice vectors are significantly smaller then the radius of the Ewald sphere [36]. Planes parallel to the zero order zone but not containing the origin are termed higher order Laue zones [34]. The first of these can be seen in Fig. 3.5.

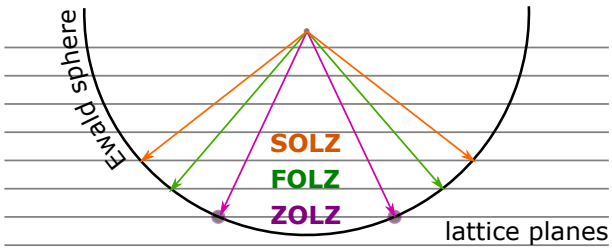

Figure 3.5: Ewald sphere intersecting a number of atom planes with the zero, first and second order Laue zones (ZOLZ, FOLZ, SOLZ). Based on [34].

Convergent beam electron diffraction

While selected area diffraction can be used in cTEM to gain information about µm sized sample regions, CBED makes it possible to probe very small regions more thoroughly than with real space imaging alone [37]. The description presented in the following chapter is based on Ref. [38].

An integral concept for understanding CBED is the excitation error. In Fig. 3.6, two incident beams $\mathbf{K}_0$ and $\mathbf{K}_0'$, that correspond to the diffracted beams $\mathbf{K}_0 + \mathbf{g}$ and $\mathbf{K}_0' + \mathbf{g}$ are shown. While the first satisfies the Bragg condition and lies on the Ewald sphere, the latter is not exactly Bragg reflected, and is given by $\mathbf{K}_0 + \mathbf{g} + \mathbf{S}_g$ with the excitation error $\mathbf{S}_g$. For a parallel sided crystal, the excitation error can be considered to be parallel to the surface normal direction and can be rewritten to

$$|\mathbf{K}_0 + \mathbf{g} + \mathbf{S}_g|^2 \approx |\mathbf{K}_0 + \mathbf{g}|^2 + 2K_0 S_g, \tag{3.8}$$

using the kinematic condition

$$|\mathbf{K}_0 + \mathbf{g} + \mathbf{S}_g|^2 = |\mathbf{K}_0|^2. \tag{3.9}$$

Because of the small scattering angles the $\mathbf{K}_0$ component along the surface normal was assumed to be K_0.

Taking $\hat{z}$ as the zone-axis direction, the incident wavevector can be written as sum of its $\hat{z}$ and tangential components $\mathbf{K}_0 = K_z\hat{z} + \mathbf{K}_t$ leading to the excitation error

$$S_g = \frac{K_t^2 - |\mathbf{K}_t + \mathbf{g}|^2}{2K_0}. \tag{3.10}$$

The deviation from the Bragg angle is calculated as $\delta\Theta \approx \Delta/(1/\lambda)$, where Δ is the change of the component of $\mathbf{K}_0$ along the reciprocal lattice vector $\mathbf{g}$. This leads to the simple relation

$$S_g = g\delta\Theta. \tag{3.11}$$

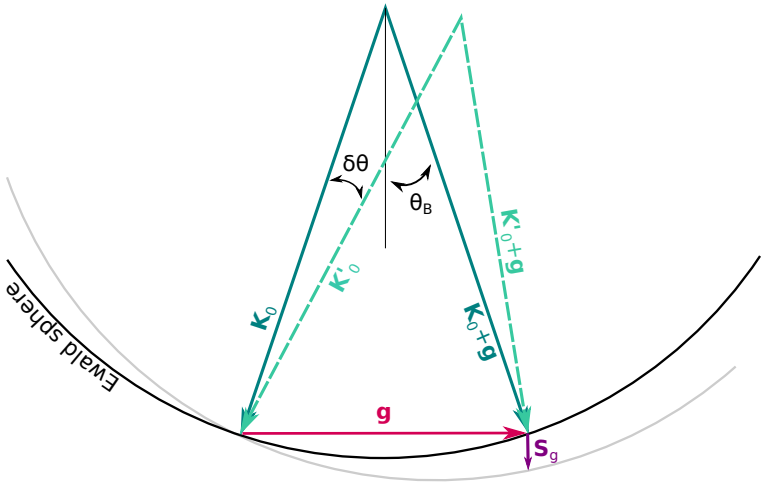

Figure 3.6: Visualisation of two incident electron beams, $\mathbf{K}_0$ in Bragg condition and $\mathbf{K}'_0$ slightly off to demonstrate the definition of the excitation error $\mathbf{S}_g$. Based on Ref. [25].

When an electron beam is focused on a sample, every specific origin point in the aperture gives rise to a family of points at the detector plane, that lie on the reciprocal lattice and are connected to the specific incident direction. Now not every origin point has to fulfill the Bragg condition exactly. When the incident direction is varied a bit, the excitation error changes, resulting in intensity changes in the diffraction disk. As seen in equation 3.11, S_g changes linearly along the reciprocal lattice vector direction with the deviation from the Bragg angle. Because the possible range of this change is connected to the length of $\mathbf{g}$, the change for higher order Laue zone reflections is more drastic then for zero order reflections. The two largest contributions to the intensity of the diffraction patterns are the excitation error and the crystal thickness, but because of the small area probed with this method the thickness can be assumed to be roughly constant and intensity variations can therefore provide useful information about the excitation error variations. The higher order Bragg reflections lead to fine features in the diffraction patterns that are very useful as they react strongly to changes in lattice parameters and strain [37].

How different points in the aperture result in different points in the resulting Bragg disks is illustrated in Fig. 3.7.

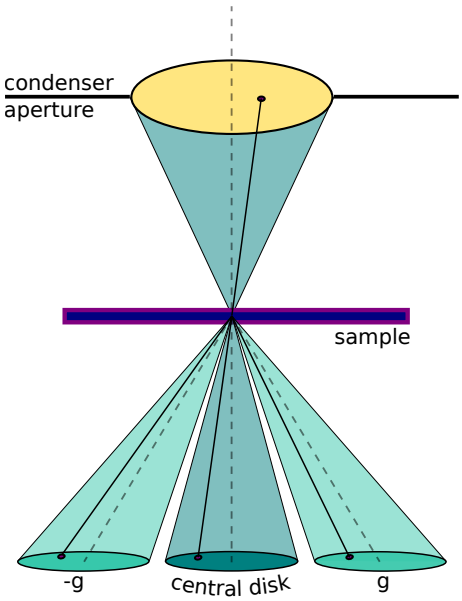

Figure 3.7: Schematic illustration showing how a point in the aperture leads to different points in the CBED discs. Figure based on Ref. [25].

3.2 Instrumentation

3.2.1 Electron guns

The first hurdle for electron microscopy is producing an electron beam that has a sufficiently small energy spread, while maintaining a sufficiently high beam current. While thermal emission tips like heated tungsten filament or LaB_6 guns have the advantage of high beam currents under moderate vacuum conditions, they have high energy spreads which makes them unsuited for delicate techniques [33]. When a narrow energy spread is needed, cold field emission guns (FEGs) can be used. There the electron extraction is achieved by applying a high tension to a sharp single crystal tungsten tip. Even though the beam currents j are small compared to the thermal emitters, the brightness [33]

$$B = \frac{j}{d\Omega} \tag{3.12}$$

is very high because of the small emitting area of the tip, leading to scattering to a very small solid angle $d\Omega = \pi\alpha^2$, where α is the scattering semiangle. To avoid damage to the tip by ion sputtering due to the high extractor voltage, UHV conditions are required at the gun [37].

3.2.2 Electron lenses

While in visible light microscopy materials with different refraction indices can be used to guide the light on convergent or divergent paths, in electron optics a lens utilizes the Lorentz force

$$\mathbf{F} = -e(\mathbf{v} \times \mathbf{B}) \tag{3.13}$$

exerted on an electron with charge $-e = -1.602 \cdot 10^{-19}$ C travelling with the velocity $\mathbf{v}$ through the magnetic field $\mathbf{B}$ to focus the electrons on a helical path [33]. The simplest electron lens is an electrostatic lens, where permanent magnets are used for focusing, with the advantage of being rotation free and easy in construction. Nowadays they are rarely used [33], so here only electromagnetic lenses will be discussed in more detail.

Electromagnetic lenses are normally constructed from two soft magnetic pole pieces with copper coils wound around them. When current is passed through the coils the focusing magnetic field is established in the gaps of the pole pieces that can be tuned via the current [34]. The simple round lens that can be seen in Fig. 3.8 a) has the disadvantage of introducing significant optical aberrations, therefore different non-rotational lens geometries have to be considered. For multipole lenses multiple pole pieces of different polarities are arranged as seen in Fig. 3.8 b), leading to a symmetry breaking and better imaging conditions [33].

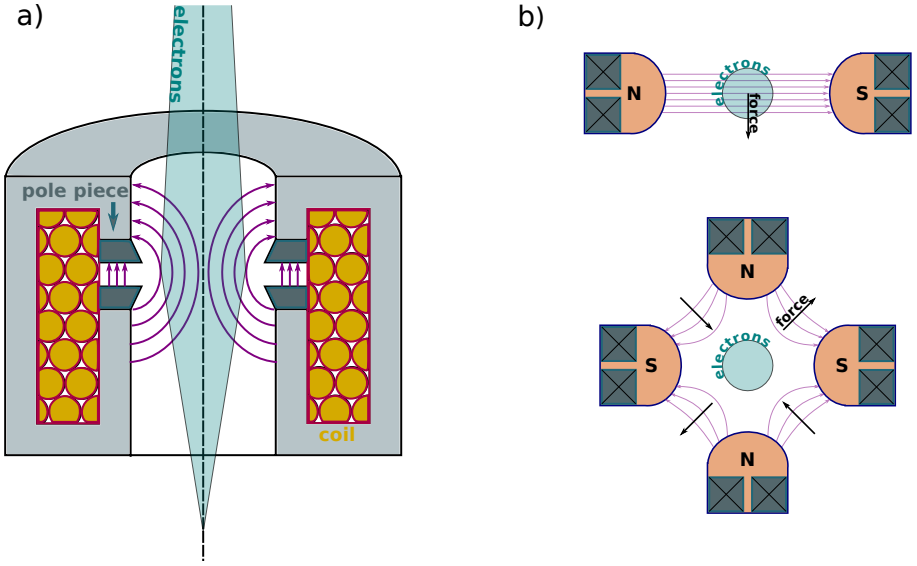

Figure 3.8: Illustration of magnetic lens design. a) A round lens. b) Dipole (upper) and quadrupole lens (lower). Different designs lead to different forces on the electrons and can therefore used to shape the beam. Figures based on [33, 34].

3.2.3 Electron detectors

Extracting electrons, passing them through complicated lens systems and forming the desired image of a specimen is a good start, but without a method to record the information all of the effort is in vain. In the beginning of TEM, photographic film was used to record analogous images, offering high resolution and good dynamic range. However,the time resolution was poor, the number of images was always limited by the photographic film available and the conversion of electron flux to recorded intensity was not linear [39]. With the rise of the digital age, other detectors that are still in use today were devised. The most commonly used electron detector for TEM is the charge coupled device (CCD) where charges are collected in a large number of metal oxide semiconductor capacitors and integrated after a certain collection time. The electrons are normally not coupled directly to the CCD, but are converted to photons beforehand by a scintillator [33]. The conversion process leads to a spreading of the beam and a blurring of the image in addition to the dark noise that influences the signal and slow readout that makes this detector unsuitable for scanning techniques [39]. This detector type is shown in Fig. 3.9 a).

The second common detector geometry is the scintillator/photomultiplier tube combination, where the electrons are converted to photons by the scintillator and a photomultiplier uses dynodes that produce many secondary electrons and lead to a gain of about 10^7. It combines all input to one output and is often used for annular detectors in STEM [33, 39]. This design is illustrated in Fig. 3.9 b).

3.2.4 Aberrations and aberration correction

As discussed above, the short electron wavelength would suggest a possible resolution in the sub-Ångström range, unfortunately this is severely limited by aberrations. Aberrations can be categorised into coherent or geometrical aberrations that stem from the lens' magnetic field and lead to a distortion of the wavefront with retained coherence, and incoherent aberrations that have different effects on waves of the same wavefront [33].

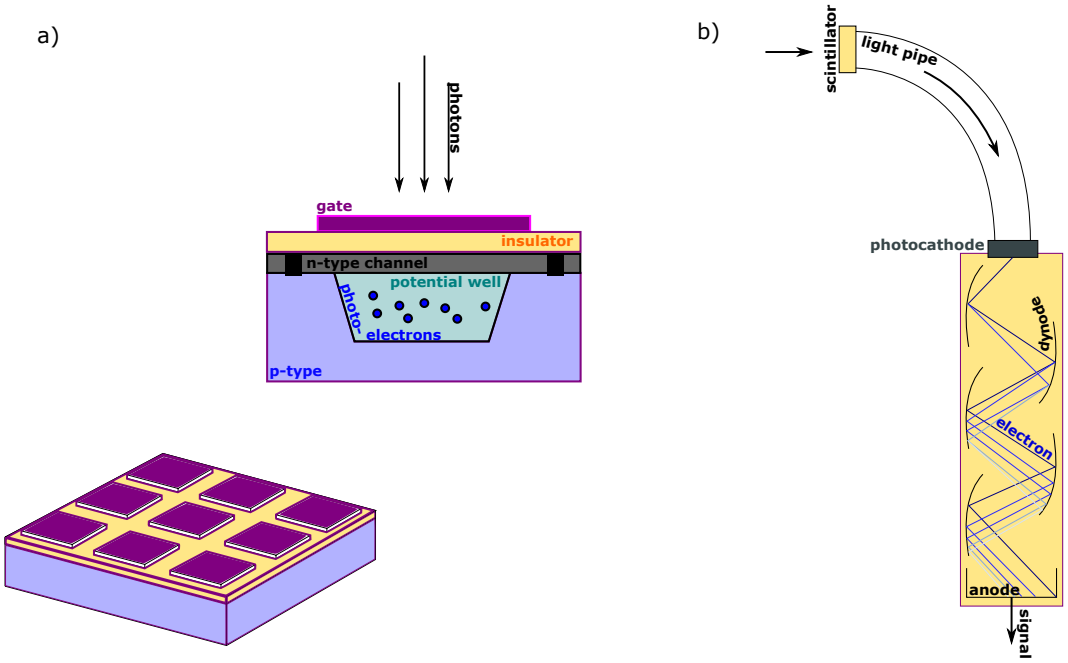

Figure 3.9: Different detector geometries. a) Principle of a CCD camera. Photons hitting the gate lead to the collection of charge in the potential well that is shifted out of the array after one frame. b) Scintillator/photomultiplier combination. The dynodes lead to a gain in signal that is then passed to the computer. Based on Ref. [25].

Geometric aberrations

Geometric aberrations can be quantified by the deviation from the ideal electron path given by the aberration function

$$\chi = \frac{2\pi}{\lambda} W, \tag{3.14}$$

where W is the error in the wavefront. This can be expanded with respect to the illumination semiangle θ giving [38]

$$\chi(\theta) = \frac{1}{2}\Delta f \theta^2 + \frac{1}{4} C_S \theta^4 + C_5 \theta^6 + \frac{1}{8} C_7 \theta^8 + \dots \tag{3.15}$$

where Δf is the defocus and C_S, C_5 and C_7 are the third-, fifth- and seventh-order spherical aberration coefficients. The third-order spherical aberration is the main resolution limit in electron microscopy and in contrast to visible light microscopy, where lenses with a positive and a negative aberration coefficient can be combined to correct this effect, magnetic lenses always have a positive spherical aberration coefficient, which leads to the need for sophisticated aberration correctors. The radius of the spherically aberrated disk in the Gaussian image plane of a real lens can be written as

$$r_{sph} = C_S \beta^3, \tag{3.16}$$

where the semiangle θ was substituted for the maximum angle of collection of the aperture β.

One strategy to minimise the effect of spherical aberration is to defocus the lens slightly from the Gaussian image plane to the plane of least confusion where the radius of the disk is quartered [34]. The effect of spherical aberration on the electron paths and the different image planes can be seen in Fig. 3.10.

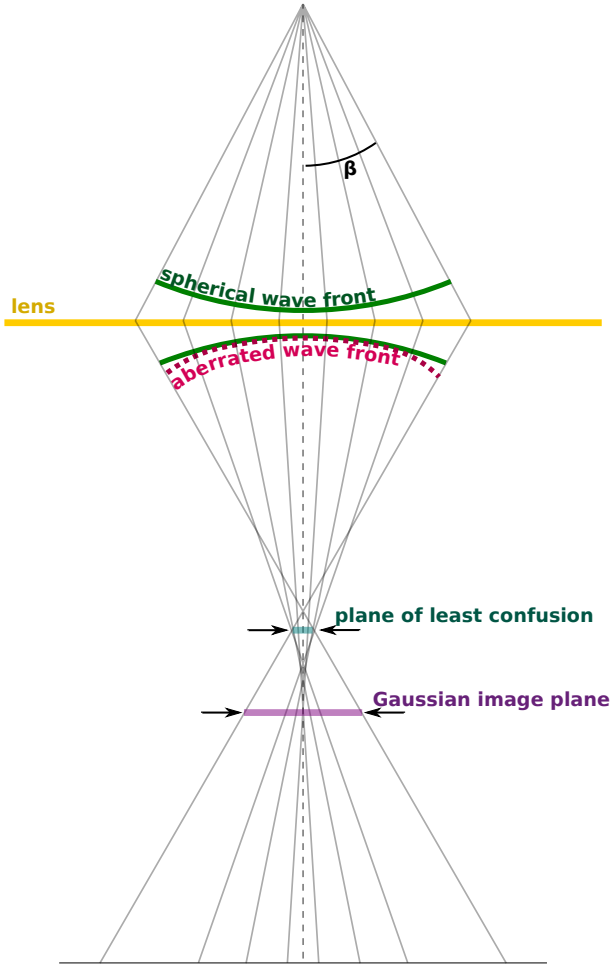

Figure 3.10: Effect of spherical aberration on the electron wavefront. Based on Ref. [34].

Spherical aberration correctors

In 1936 Otto Scherzer proved [40] the impossibility to eradicate spherical aberration in an electron optical system if all of the following conditions are fulfilled at once: (1) rotationally symmetric optical system, (2) a real image of the object is produced, (3) the electromagnetic fields are static, (4) the optical axis is free from charges. Modern correctors mostly rely on the breaking of the rotational symmetry by using multipole lenses where an even number of magnetic north and south poles are arranged around the optical axis of the lens leading to the field lines being increasingly

perpendicular to the electron beam therefore introducing less rotation and more deflection of the electron trajectories. One corrector design is the quadurpole-octuple corrector that consists of four quadrupole lenses and three octupole lenses arranged in a sophisticated fashion, resulting in a negative spherical aberration coefficient that negates the positive spherical aberration introduced by the objective lens. However, in achieving this, strong astigmatism is introduced as a parasitic aberration that has to be corrected afterwards [33]. This corrector scheme is illustrated in Fig. 3.11.

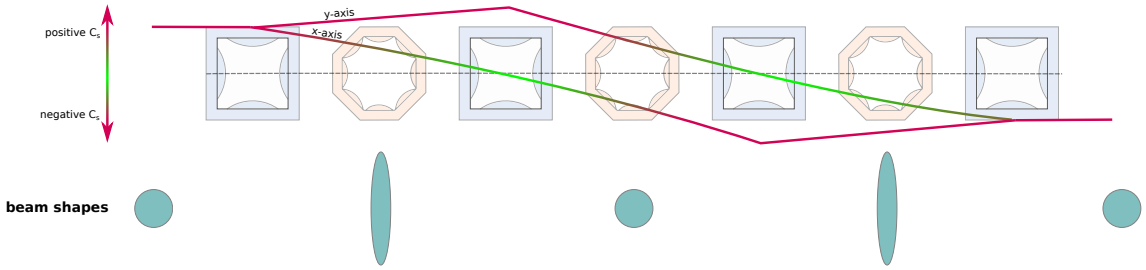

Figure 3.11: Schematic of a quadurpole-octuple corrector. The quadrupoles and octupoles are represented by squares and octagons respectively and the spherical aberration coefficient depending on the position in the corrector is shown separately for the x and y direction. Also the beam shapes at the different positions are indicated in teal at the lower part of the image. Based on Ref. [33].

Chromatic aberration

When the spherical aberration is corrected, chromatic aberration, the variation of the lens effect due to energy spread of the beam, becomes relevant. As seen above, the energy spread can be minimised by choosing the right electron source and further reduced by introducing a monochromator in the beam path. Electron filtering can be used for correcting chromatic aberrations introduced by thick specimen in high resolution TEM, but for thin specimen, this is not necessary and will not be discussed further.

Astigmatism

Astigmatism arises from non-uniformities in the lens magnetic fields due to inhomogenities in the pole pieces of the lenses and slightly off-center or contaminated apertures. However this is relatively easy to correct using octupole lenses that create compensating fields negating the deviations due to astigmatism.

3.2.5 Resolution

The resolution, or more accurately the minimum-resolvable distance of a microscope determines the minimum size of still distinguishable features. Diffraction and lens imperfections lead to a broadening of the point source to a Gaussian image with a radius limiting the resolution.

A method of quantifying resolution is the Rayleigh criterion where two sources are assumed to be resolvable when the intensity maximum of one overlaps with the first minimum of the other. With this criterion the minimum-resolvable distance without aberrations is given by the theoretical radius of a point source broadened to an Airy disk by diffraction

$$r_{th} = 1.22\frac{\lambda}{\beta}, \tag{3.17}$$

where β describes the maximum angle of collection of the aperture. In reality spherical aberration has a strong influence on the resolution and the radius r_{sph} of the spherically aberrated disk in equation .3.16 has to be taken in account leading to a disk radius of

$$r = (r_{th}^2 + r_{sph}^2)^{1/2}. \tag{3.18}$$

If an ideal collection angle is selected, a minimum-resolvable distance of

$$r_{min} \approx 0.91(C_s\lambda_e^3)^{1/4} \tag{3.19}$$

can theoretically be reached. For typical TEM instruments this value ranges from about 0.25 nm to 0.3 nm [34].

As mentioned above, chromatic aberration also limits resolution, but as this becomes a problem mostly for thicker samples it is neglected here.

3.3 Scanning transmission electron microscopy

STEM uses a convergent electron probe to scan over the sample area, leading to images with pixels representing the counted electrons arriving at the detector for every probe position.

STEM setup

A typical STEM setup can be seen in Fig. 3.12.

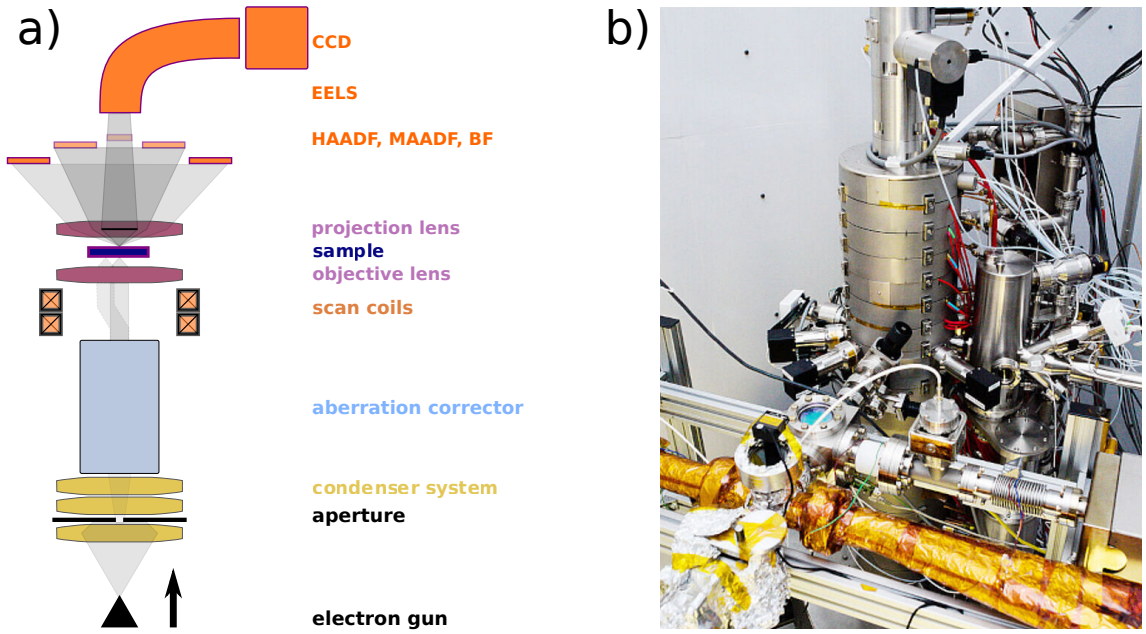

Figure 3.12: Schematic illustration of a typical STEM setup on the left hand side. The right hand side shows a photograph of of the Nion UltraSTEM 100 in Vienna (from Ref. [41]).

The electron beam is extracted from the electron gun often located at the bottom and accelerated into the condenser system consisting of multiple lenses. A Gaussian image of the source is formed and passed to the aberration corrector. Scan coils then modify the beam path before it is passed through the objective aperture and focused onto the sample by the objective lens. After the sample various detectors are mounted. A small circular detector on the optical axis is used to record bright field (BF) images from weakly scattered electrons while medium angle annular dark field (MAADF) and high angle annular dark field (HAADF) detectors collect strongly scattered electrons leading to easy to interpret Z-contrast images. The angular ranges of the MAADF and HAADF detectors in the Nion UltraSTEM 100, our aberration corrected instrument in Vienna, are 60 mrad to 200 mrad and 80 mrad to 300 mrad, respectively [33]. Also a CCD camera as well as an electron energy loss spectrometer are typically mounted on STEM instruments.

Here the discussion will be centred around MAADF imaging, as this was used for the experiments.

3.3.1 Probe formation

The electron probe describes the demagnified image of the source and is an important factor for the minimum resolved distance for STEM devices.

The source can be quantified by it's brightness as described by equation 3.12 and the probe size

can be estimated as a sum of the diffraction-widened probe radius r_{diff} and the source image radius r_{src} as [42]

$$r \approx \sqrt{r_{diff}^2 + r_{src}^2}. \tag{3.20}$$

When including aberration effects in the calculations and optimising the probe angle depending on the beamcurrent, a minimum probe size can be calculated that strongly depends on the aberration coefficient and the wavelength. Before aberration correction was standard, high acceleration voltages were often used to optimise the resolution by minimising the wavelength, however this is not ideal because of the high knock-on damage in these regimes [33].

Also the probe size is a trade off between signal-to-noise ratio and resolution, as the optimised semiangle implies the use of small apertures that cut away much of the signal. The theoretically best probe size would occur at the limit of zero beam current where there is of course no signal anymore [38].

3.3.2 Image formation and contrast

After the electron probe (described by a function $\psi_P(\mathbf{R} - \mathbf{R}_P)$ at position $\mathbf{R}_P$) interacts with a sample (described by the transmission function $\phi(\mathbf{R})$ at a point $\mathbf{R}$), the far field wave function, i. e., the wave function seen by the detectors, can be calculated as a Fourier transform of their product which is equivalent to the convolution of the separately Fourier transformed probe and transmission functions.

By Fourier transforming the probe function the aperture function $A(\mathbf{K}_p)\exp(\mathrm{i}\mathbf{K}_P\mathbf{R}_P)$ can be calculated. The exponential here describes the positional shift to the probe position $\mathbf{R}_P$, and the factor $A(\mathbf{K}_p)$ includes aperture and aberration effects. The Fourier transform of the real space transmission function consists of a number of sharp peaks for the atom sites with amplitudes ϕ_g for each of it's Fourier components.

The final far field wavefunction is given by the convolution of these terms that turns out to be a discrete sum over all diffraction discs as illustrated in Fig. 3.13. The contrast in STEM is a result of the interference features of overlapping disks [33].

There are two very distinct imaging modes in STEM, coherent BF and incoherent ADF imaging, that differ in the angular ranges and geometry of the detectors. BF detectors are typically circular and located directly at the optical axis. They have areas that are small compared to the

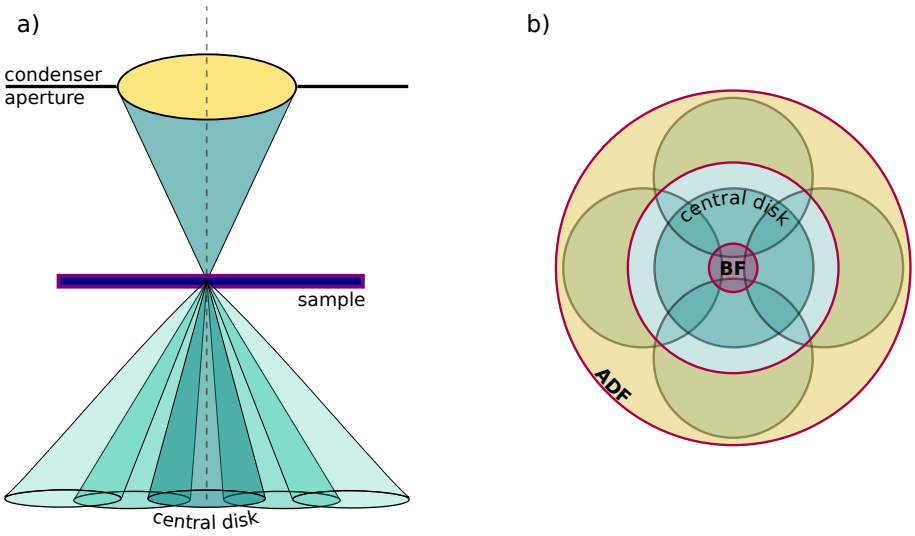

Figure 3.13: a) Schematic illustration of diffraction disks resulting from a STEM probe hitting the sample. b) Illustration of the ADF and BF detector geometries with respect to the diffraction disks.

interference fringes resulting from overlapping disks, so the resulting images depend strongly on the position of the features and are sensitive to phase information. The larger ADF detectors are located with a specific inner and outer radius around the optical axis and their areas are large enough to integrate over the fringes and therefore eliminate the phase sensitivity.

For bright field imaging the intensity at the detector can be written as a convolution of the wave function and the transmission function,

$$I_{BF}(\mathbf{R}_P) = |\psi_P(\mathbf{R}_P) \otimes \phi(\mathbf{R}_P)|. \tag{3.21}$$

The same equation describes by the principle of reciprocity also phase contrast in high resolution TEM imaging.

The incoherent ADF imaging is a convolution of the probe intensity and an object function $O(\mathbf{R}_P)$ that depends on the scattering ability of the object,

$$I_{ADF}(\mathbf{R}_P) = |\psi_P(\mathbf{R}_P)| \otimes O(\mathbf{R}_P). \tag{3.22}$$

Here only intensities are involved, not relative phases, and this leads to easy to interpret images where the contrast is solely determined by the atomic number Z and the thickness of the layer. This proves an advantage over TEM and BF imaging where contrast reversals can make interpretation difficult [33].

The atomic Z-contrast can be understood starting with a single scattering atom in the beam path. If the atom is absent, all electrons pass undisturbed, therefore no intensity is registered by

the annular detector. If the atom is present in the beam path, scattering occurs following the Rutherford model with a certain screening of the Coulomb potential leading to a bright contrast proportional to Z^{α}, where $1.5 < \alpha < 2$. Often $\alpha = 1.7$ is assumed [33].

3.3.3 Limitations of conventional STEM

Even though STEM is doubtlessly a powerful method, it has a number of limitations.

For one, while there are different imaging modes available in STEM, that can for modern setups even be switched during the experiment, detector configurations like the inner and outer radii for the annular detectors are fixed within one experiment [43]. Another relevant limitation is the fairly high required dose, which can lead to beam damage inflicted to the material by the electron probe. For beam sensitive samples the electron dose needed to gain useful information with STEM can be too much for the material to withstand and structural defects can become very problematic [44]. Moreover, the strong Z-contrast in ADF STEM prevents the imaging of light and heavy elements next to each other [45].

3.4 4D scanning transmission electron microscopy

In STEM measurements the probe is moved over the sample, creating a CBED pattern at every position. In conventional STEM imaging, however, only a fraction of the information contained in this pattern is actually used. The normal STEM detector geometries integrate over a specific region of the pattern and much of the information contained in the pattern is lost, as only one value proportional to the sum of all electrons in that region is registered. While this has a lot of advantages, another possibility is to record the whole diffraction pattern at every probe position. Because this procedure leads to a 4D datacube, a 2D array of probe positions, each containing another 2D array of the CBED pattern, it has become known under the term 4D-STEM [43].

3.4.1 4D-STEM detectors

One reason why 4D-STEM has not been practised a lot until a few years back is the limitation in the available detectors. As discussed above, the standard for most STEM devices is a CCD camera, that has a readout speed of $\leq$60 frames/s, which is too low to effectively record

4D-STEM data [43]. Also, CCD cameras have high pixel densities but low dynamic ranges, as they are specifically designed for real space imaging, where information is detailed but spread out and intensities lie in a narrow range. However, for diffraction imaging, a completely different geometry is better. Diffraction peaks are very localised and distributed sparsely but there are large intensity differences. So detectors with lower pixel densities are sufficient as long as the dynamic range is high enough. At the same time, this leads to a reduction of recorded data at each probe position [46]. Different detector designs have emerged over the last years including hybrid pixel array detectors that convince with their high dynamic ranges, single-electron selectivity and good readout speeds [43].

3.4.2 4D-STEM imaging modes

With the massive amount of data acquired, a crucial question arises: How can these diffraction patterns be interpreted?

Other than with conventional ADF STEM, to get useful information from 4D-STEM datasets a non-negligible amount of computational resources has to be used, their complexity differing significantly depending on the information required from the raw data. In the following, different imaging modes of 4D-STEM are explained.

Virtual detectors

'Normal' annular/circular detectors work by integrating all electrons scattered in a specific angular range. With a diffraction pattern recorded at every probe position, the same principle can be applied to generate any virtual detector within the range of the physical pixelated detector by adding up the electrons in that range for every single recorded diffraction pattern [43]. This is illustrated in Fig. 3.14.

This way of imaging has the great advantage that, other than with 'real' detectors, the collection angles can be configured freely after data acquisition. Here solely the angular range of the pixelated detector is the limiting factor, so high angle annular dark field images can present a problem [43].

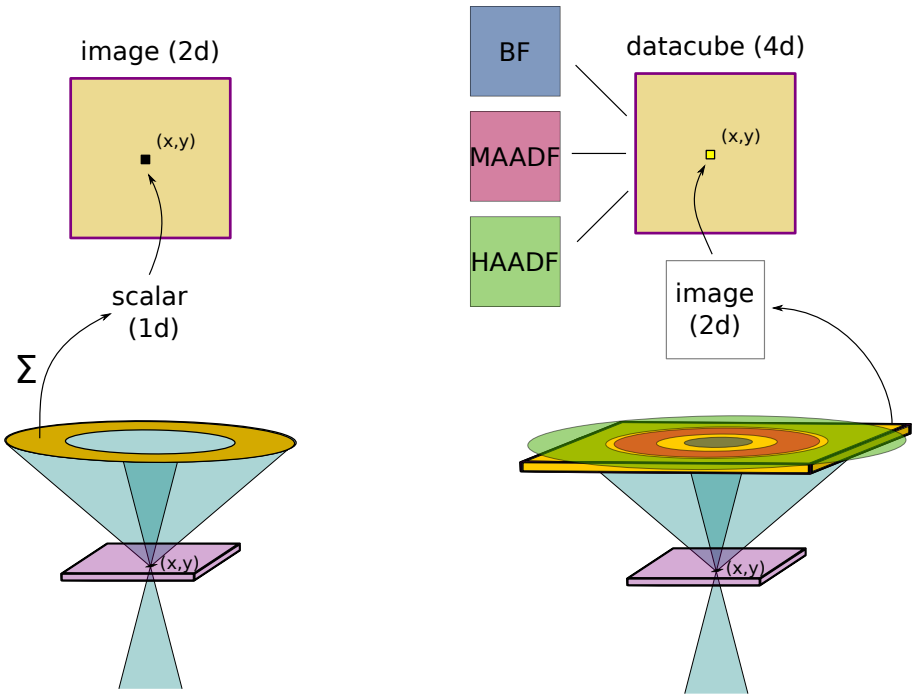

Figure 3.14: Illustration of the difference between ADF STEM (left) and 4D-STEM imaging (right). While for ADF STEM all electrons hitting a detector of well defined geometry are integrated giving one value for every pixel and resulting in a 2D image of the scanned region, in 4D-STEM, the detector records a whole 2D diffraction pattern at every scan position resulting in a 4D datacube of the scanned region. This datacube can for example be used to create virtual images by applying some detector geometry.

Differential phase contrast imaging

As discussed above, typical ADF imaging in STEM and the associated easily interpreted Z-contrast is a consequence of incoherent scattering to higher angles where only intensities are involved.

Phase contrast, however, can provide more detailed information on the sample, but even though it is possible to gain phase information by using the BF in STEM, conventionally this provides only poor contrast because of the efficient aberration correction that is necessary for incoherent imaging but not ideal for BF phase contrast imaging. The reason for this is, that without aberrations, transferred wavefunctions at two opposite points in the diffraction pattern have phases of equal amplitude but opposite sign and the summation over a central-symmetric detector geometry results in vanishing phase contrast [47].

The idea of differential phase contrast (DPC) imaging is to gain information on the momentum change of the STEM probe passing through the sample, and therefore also on local electric fields.

To this end, data is recorded on segmented detectors and the signal of opposed segments is subtracted, giving image contrast corresponding to the gradient of the phase change through the sample [48].

In practice this has been evolved to detectors with 8 [47] or even 16 [49] segments, but using a fixed arrangement of segments is not optimal because of the limited spacial frequencies that can be probed. Also here 4D-STEM can prove to be a valuable method, as the momentum change can be calculated between all pixels in center of mass (COM) measurements [43]. Because the COM image corresponds to the projected electric field, its integrand gives information about the potential and it's derivative about the charge density [44].

Ptychography

While DPC images contain more information about the sample than regular incoherent ADF STEM images, there is still significant room at the top – the goal would be reconstruction of the whole phase information from the collected data. With 4D-STEM and ptychography that can be realised [43]. The idea of ptychography was first described by the German physicist Walter Hoppe in 1969 in a series of three papers [50] where he discussed reconstructing a periodic structure from recording coherent CBED patterns measured in the far field. As discussed before, the phase cannot directly be retrieved from the measured intensity, but Hoppe developed a method to use the interference of the overlapping Bragg peaks in the CBED to reconstruct phase information provided there is enough ambiguity in the data. The name ptychography consists of the greek $\pi\tau\upsilon\chi\acute{\eta}$ (ptukhe) which means *fold* and the word $\gamma\rho\acute{\alpha}\varphi\omega$ (grapho) which means *to write*. The word *fold* was chosen because of the German term *Faltung* (so folding) for convolution [51].

3.4.3 Ptychotomography

Conventional microscopy techniques can only be used to obtain 2D information because solely the projected potential of the sample is relevant.

Many tomography methods that have been developed for solving the 3D structure of bulk materials can not be applied to thin samples, as they either require a high dose or have very specific requirements for the specimen [3].

A method that has been shown by Hofer et al. in 2018 [52] to enable the extraction of 3D

information of thin films is few-tilt electron tomography. There differently tilted ADF images are recorded and an atomic model is iteratively adjusted to get a realistic simulation of the out-of-plane structure from the projection. While this has been effectively used with down to two tilt images, it can be further optimised by employing 4D-STEM and ptychography, as Hofer et al. have shown in further work [3].

As discussed above, ptychography utilises the most information from the data sets, therefore improving dose efficiency and distinguishability of light and heavy atoms which leads to higher precision tomography results, especially for complex materials [3].

3.5 Experimental implementation

3.5.1 Preparation of monolayer graphene samples

First, monolayer samples are prepared using easy transfer graphene purchased from Graphenea™ [53], that is transferred to silicon nitrate TEM grids from Silson [54] with a membrane size of 0.09×0.09 mm and 3×3 windows and membrane and frame thicknesses of 1 and 200 µm, respectively. The windows of the SiN grids are marked in binary as seen in the visible light microscopy images in Fig. 3.15.

The PMMA/graphene layer is first detached from the stabilisation substrate by submersion in deionized water and then fished out with the TEM grid before drying in ambient conditions at room temperature for 30 min and on a heating plate at 150 °C for another 60 min. The PMMA is then removed using subsequent warm acetone and room temperature isopropanol baths for 60 and 90 min, respectively. The process is described in more detail on the Graphenea™ product page [53] and shown in Fig. 3.16.

3.5.2 Sample alteration and study in the CANVAS system

The undistorted alteration and subsequent study of samples is only possible if they are kept in UHV during the whole process, as exposure to ambient conditions leads to immediate contamination with, e.g., hydrocarbons. The instrumentation allowing such experiments at the University of Vienna is the Controlled Alteration of Nanomaterials in Vacuum down to the Atomic Scale (CANVAS) system [55]. Here up to three samples can be stored indefinitely in 'cars', that can

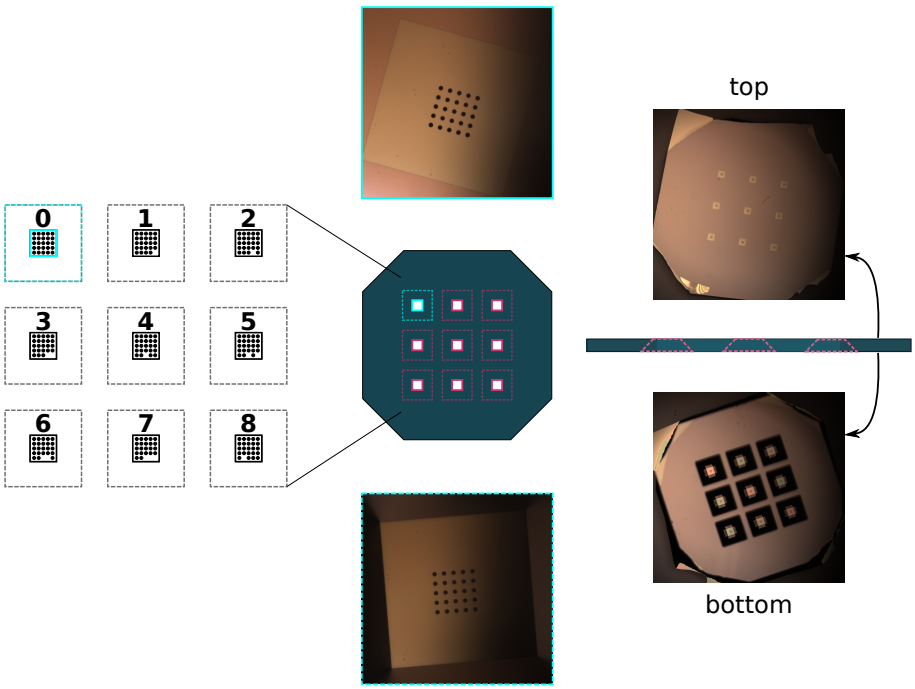

Figure 3.15: Illustration of SiN TEM grids. The central panel shows a schematic of a SiN TEM grid with 9 windows, each containing a number of holes where the sample is suspended. The squares are numbered using the binary system as seen in the diagram on the left hand side. The right hand side shows visible light microscopy images of the top and bottom of a silicon nitrite grid while the centre top and bottom panels show images of a single window of such a grid.

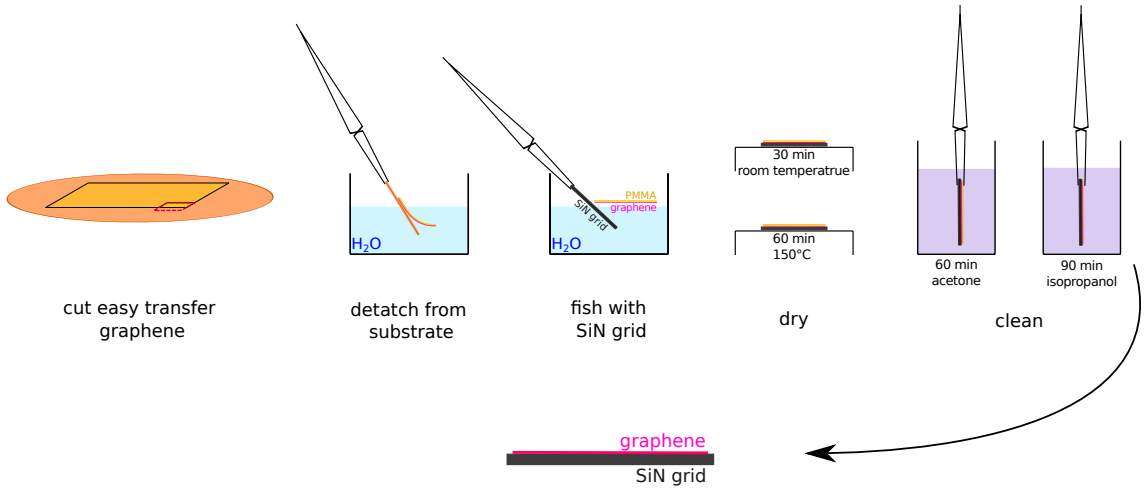

Figure 3.16: The sample transfer process. First a piece of the sample consisting of purchased stabilising substrate, graphene and PMMA is cut and submerged at an angle into deionized water. The graphene/PMMA stack separates from the stabilising substrate and can be picked up with a TEM grid. It is then dried and cleaned in acetone and isopropanol alcohol to disolve the PMMA.

be manoeuvred freely between different devices connected with UHV pipes by use of magnets. A schematic illustration of the CANVAS system can be seen in Fig. 3.17.

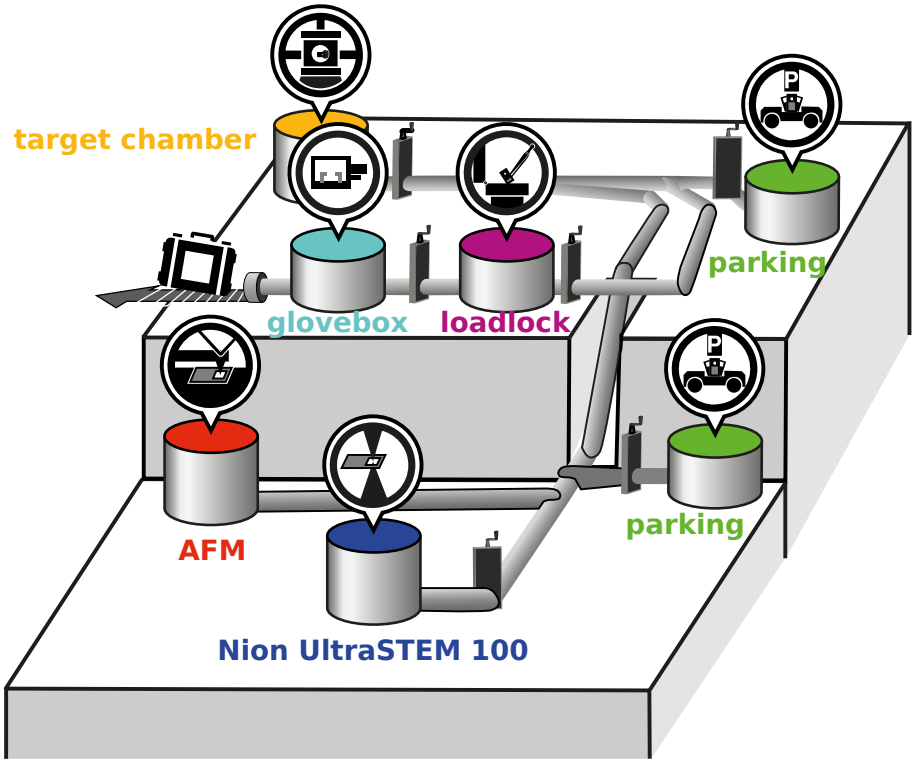

Figure 3.17: Schematic illustration of the CANVAS system located at the Sternwarte laboratory in Vienna. The relevant instruments for this project are the loadlock, the target chamber and the Nion UltraSTEM 100. The graphic was created by Arron Huele and updated by Manuel Längle and Clara Kofler.

For this thesis, the loadlock, the laser located in the target chamber and the Nion UltraSTEM 100 are relevant and will be described in the following.

Loadlock: Introducing the sample to the system

The loadlock is the front door to the house that is our UHV system. It consists of a chamber that can be flooded with argon and is closed off from the rest of the CANVAS system by a double gate, so two subsequent valves, to assure the integrity of the vacuum in the rest of the system. Once flooded, the chamber can be opened from the outside to introduce new samples to the system. They are clamped onto so-called pucks that fit into the transport cars. After sample exchange the chamber is sealed again and baked at temperatures up to 180 °C in vacuum.

Target chamber laser: Cleaning and formation of folds

The target chamber consists of a plasam source and deceleration setup for ion irradiation, as well as a SHS-4500 Laser Diode Driver from Lasertack Gmbh (up to 6 W, 445 nm wavelength). A schematic illustration of the setup is shown in Fig. 3.18.

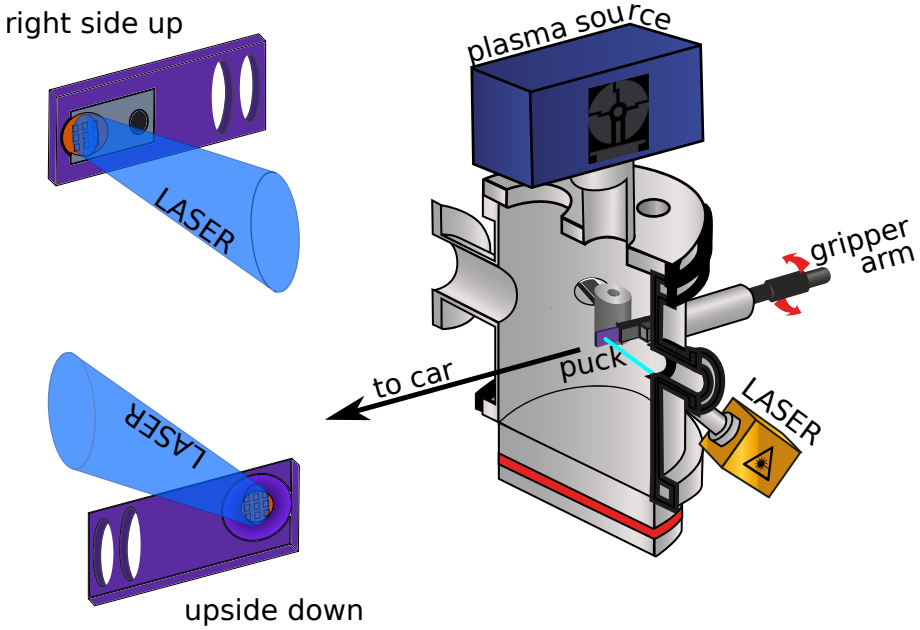

Figure 3.18: Schematic illustration of the target chamber. For this work, the relevant functionality of the target chamber is the laser that can be focused on the sample on the puck. Graphic created by Arron Huele and modified by Manuel Längle and Clara Kofler.

The puck containing the sample is removed from the car using a gripper arm and brought into the path of the laser. After alignment and warm up, the desired power is selected and the sample can be lasered for a chosen amount of time.

This process is used mostly to 'clean' samples, i.e., remove contamination through heating. However the heat has the additional effect of graphene contracting due to its negative thermal expansion coefficient, leading to folds with bi- and trilayers.

Here the samples have been lasered using 27% or 42% of the maximum laser power of 6 W for 40 min, giving large clean monolayer regions as well as folds of bi- and trilayer regions. Using the laser for 6 min at 27% power before every microscopy session does not notably change the structure of the sample, but reduces the amount of mobile contamination while imaging, which would make the recording of maps impossible.

As imaging of samples on SiN grids in the Nion UltraSTEM 100 microscope is not possible in the

standard orientation currently, the samples have to be mounted upside down into the pucks to record images. This however leads to the need of lasering the samples from the 'wrong' direction. Pucks have a conical notch terminating at the sample, where the laser has to be focused in that case. This makes it difficult to adjust the laser and prevent it from being reflected off by the surrounding metal.

Nion UltraSTEM 100: Imaging

For imaging the aberration corrected Nion UltraSTEM 100 microscope was operated at 60 kV with the sample at UHV conditions.

For acquisition of characterisation images, a MAADF detector with an inner radius of 60 mrad and an outer radius of 200 mrad and an electron probe with a convergence semiangle of 30 mrad was used. Dwell times of between 8 and 16 µs and image sizes between 1024 $\times$ 1024 and 4096 $\times$ 4096 px were most common.

Once small angle regions were identified using MAADF images, the Orca CCD camera of the instrument was used with a binning factor of two to record defocused probe CBED patterns. Only the inner 750 $\times$ 750 px of the camera were recorded and the exposure time was set as 100 ms before maps with 8 $\times$ 8 nm fields of view were recorded, each with a size of 100 $\times$ 100 diffraction patterns. The size of the 4D datacube therefore corresponds to 100 $\times$ 100 $\times$ 750 $\times$ 750 = 5625 $\cdot$ 10^6 values.

The whole process would have been more accurate and less time intensive, if a direct electron detector had been used. The inclusion of the new instrumentation into the old setup has not yet been finished however. Therefore, the here recorded maps serve as an indication of what to expect from experiments conducted in the future.

3.6 Data analysis

The data analysis was done with (partly) self-written python code that can be found at Ref. [56].

3.6.1 Scaling of the images

For image scaling the fourier-scale-calibration package by Jacob Madsen [57] was used. Here the scale is calculated by detecting the Fourier spots that correspond to the scattering angles determined by the known graphene structure.

3.6.2 Determination of the twist angle

The twist angles of the bilayer regions were determined using the Fourier transformation of real space ADF images with code based on an algorithm for detecting TEM diffraction spots by Rajendra Singh. A number of parameters for the detection of the fast Fourier transform (FFT) spots have to be adjusted for every image to assure proper functionality. Once the spots are selected, the angles between the neighbouring spots are calculated and their mean is returned.

3.6.3 Analysis of the defocused CBED patterns

The method used was adapted from Ref. [5] and utilises the difference in scattering by the two twisted layers.

As discussed above, scattering of a convergent probe at a sample leads to Bragg disks at scattering angles dependent on the energy and structure as seen in Fig. 3.19 a).

When the probe is not directly in focus, but defocused to some amount Δf, the scattering leads to the displacement of the diffracted beams away from the optical axis in the direction of the corresponding Bragg disk and the effective formation of two point sources with a distance D proportional to the magnitude of the defocus. This can be seen in Fig. 3.19 b). For twisted bilayer samples, the diffraction direction of the layers differs by the twist angle and the focal points for the layers are displaced by the distance δ, that is perpendicular to the displacement D as illustrated in 3.19 c). These focal points again act as coherent point sources and form separate Bragg disks. If he twist angle is small enough, the disks overlap, resulting in interference patterns containing information about the sample structure. The situation is illustrated in Fig. 3.19 d).

Theoretically the whole in-plane structure, as well as the twist angle and interlayer spacing could be reconstructed from the angle, phase and wavelength of these interference fringes. This thesis

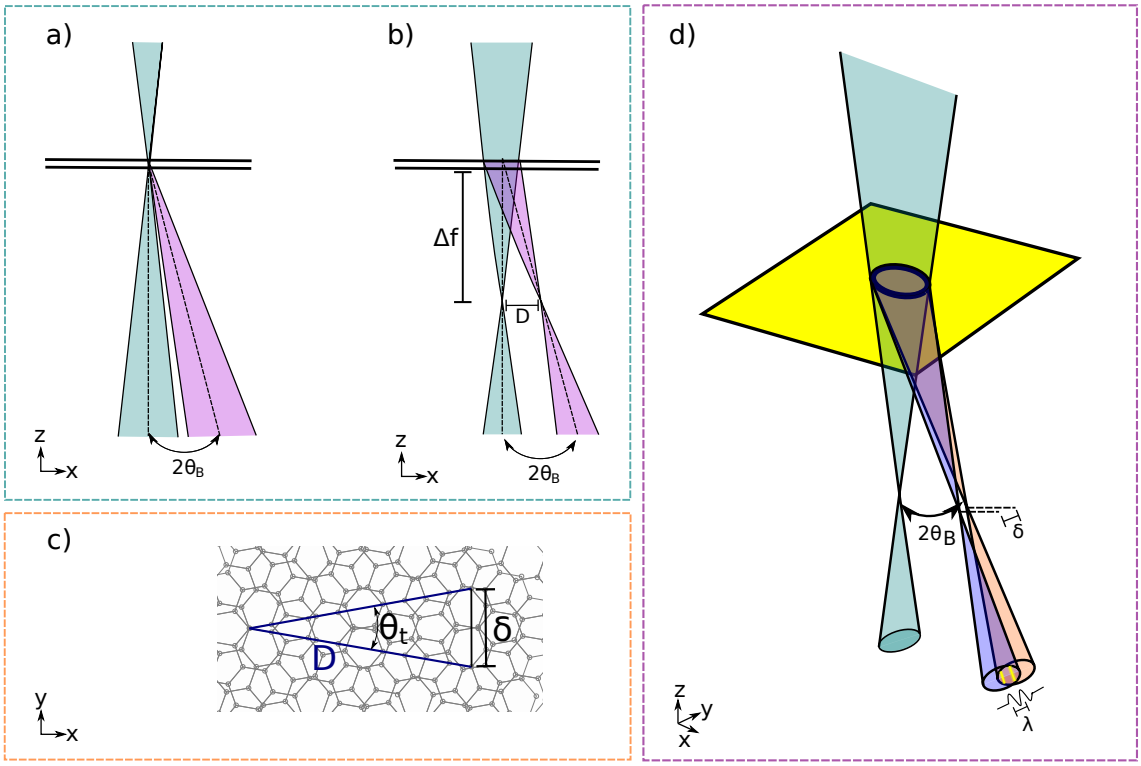

Figure 3.19: Schematic illustration of focused and defocused CBED. a) A focused beam hits the sample leading to first order diffraction spots in the angular distance of $2\theta_B$ from the transmitted beam. b) An underfocused beam hits the sample with a defocus of Δf. c) The influence of the twist angle of bilayer structures on the separation of the second order point sources. d) An overview of the whole situation and the resulting interfering Bragg disks.

concentrates on the extraction of 3D information from the data, so only the relationship of the defocus and interlayer distance with the interference patterns is discussed and analysed in detail.

As mentioned above, the reason for the interference patterns is the displacement δ of the focal points, effectively giving two point sources. This situation is equivalent to a double slit experiment, where the angular separation of the interference fringes is given by

$$\theta_\lambda = \frac{\lambda_e}{\delta}, \tag{3.23}$$

where λ_e is the electron wavelength dependent on the energy [58]. With consideration of Fig. 3.19 and using the small angle approximation $\tan 2\theta_B \approx 2\theta_B$, the relation

$$\theta_\lambda = \frac{\lambda_e}{4\theta_B \Delta f \sin \theta_t/2}, \tag{3.24}$$

depending on the Bragg angle θ_B, the twist angle θ_t and the defocus Δf, can be found. This can be used for direct calculation of the defocus value of the data.

Also the interlayer distance can be discerned from the diffraction patterns. As seen in Fig. 3.19 c), the twist angle of the layers results in the displacement of the point sources, that leads to the interference patterns. However the layers are also separated in z-direction, therefore the focus points of the two layers have a slight separation in the x-direction, as effective defocus is different for the first and the second layer of the structure as seen in Fig. 3.20 a).

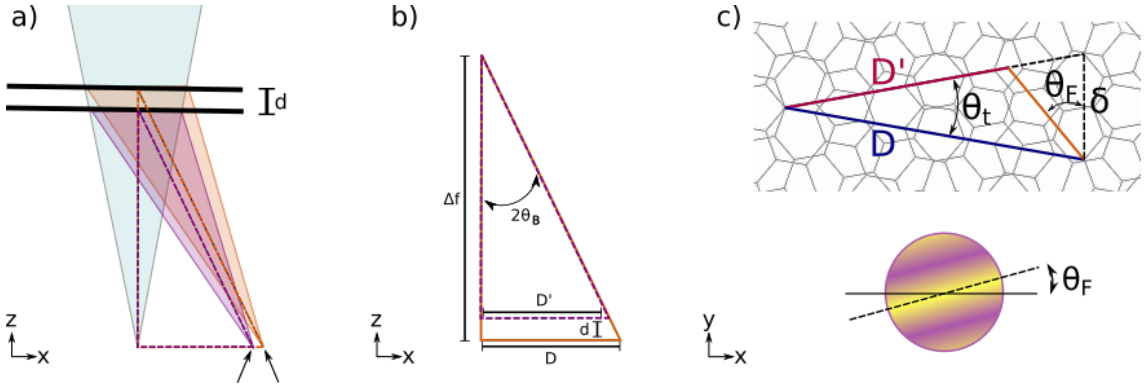

Figure 3.20: Influence of the layer separation on the diffraction patterns. a) The separate layers result in two different focus points marked by arrows. b) The triangle shows the geometric relationship between the defocus Δf, the different focus point distances D and D' from the optical axis and the interlayer distance d. c) Change of the focus point separation and resulting rotation of the interference fringes.

This difference leads also to a change in the displacement of the focal points originating from the twisted layers as illustrated in Fig. 3.20 c), and the rotation of the fringes away from the central direction by an angle θ_F.

By considering the geometry shown in Fig. 3.20 b) and c) the following relation for the interlayer distance d can be found

$$d = 2\Delta f \tan\theta_F \sin\theta_t/2. \tag{3.25}$$

Implementation

The workflow of the analysis was as follows. After loading the diffraction map using the python packages h5py and dask, the mean pattern was calculated and a threshold applied to find the bright central spot. The position and radius of the central spot were used as a first estimate for the centre and size of the convergent angle. An example of single diffraction pattern as well as the mean diffraction pattern are shown for the simulated dataset in Fig. 3.21 a). Then a threshold

was applied to a part of the images (the first 59 and 1200 diffraction patterns for the simulated and experimental datasets respectively) and the thresholded arrays were summed, giving an image where the separate disks could be well distinguished. This was again thresholded and the centre of mask positions of the regions were calculated to give an estimate of the distance of the Bragg disks from the centre and their angles. By fitting a hexagon to these estimated positions, more accurate values for the centre of the diffraction pattern and the Bragg disks could be found. The thresholded image with the the fitted disk centres is shown in Fig. 3.21 b) for the simulated dataset.

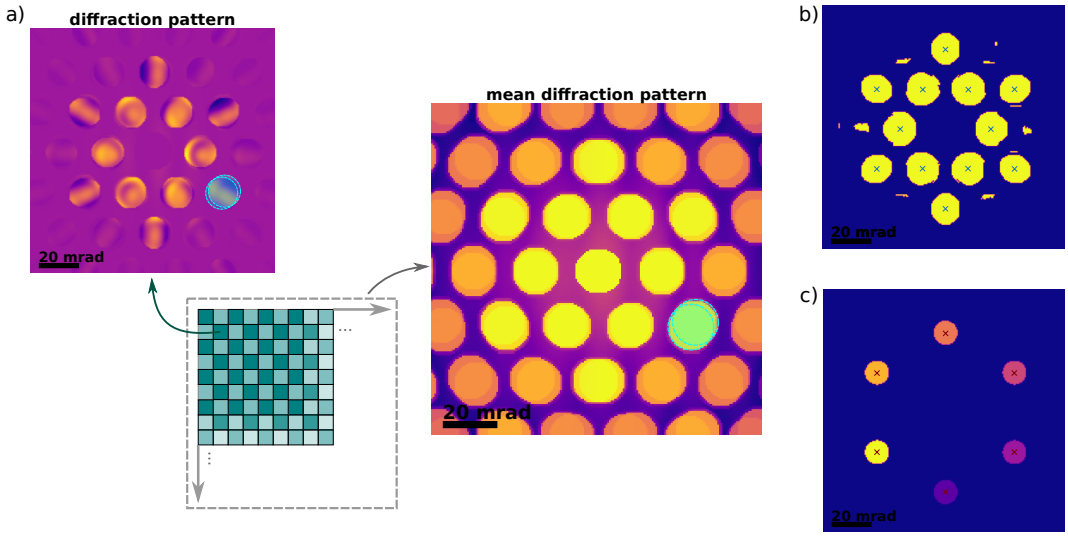

Figure 3.21: Pre-processing of the 4D datasets. a) An example diffraction pattern with the central spot masked. Two overlapping Bragg disks are marked in blue. The mean diffraction pattern shown in log scale in the centre is subtracted from every pattern before analysis to eliminate effects of the central beam that is also masked in the images. b) The detected centre spots of the scattered disks are marked in blue on the thresholded image. c) The resulting label image that is used to select the relevant disks for every analysed pattern.

From the distances of the Bragg disks from the centre, the scale of the images was then found by using the Bragg scattering rule

$$n\lambda_e = 2d \sin \theta_B \tag{3.26}$$

with the scattering order n, the wavelength λ_e, the Bragg scattering angle θ_B and the real space distance of the planes d [59].

The inner and outer reflections of graphene correspond to the armchair and zig zag planes that are illustrated in Fig. 3.22.

The distance of the armchair planes is given by $d_{ac} = a/2$ and corresponds to the diffraction

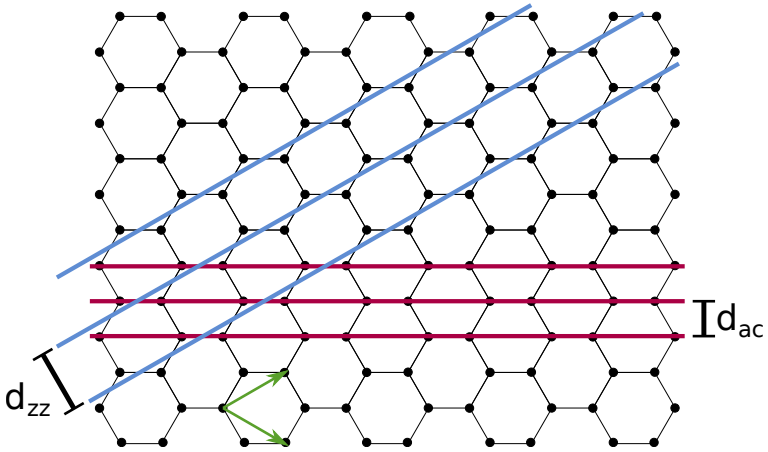

Figure 3.22: Armchair and zig zag planes in the graphene lattice in red and blue, respectively. The green arrows mark the lattice vectors.

disks farther from the centre, while the zig zag planes are separated by $d_{zz} = a \sin \pi/3$. Here $a = |\mathbf{a}| = \sqrt{3} a_{c-c}$ is the lattice constant of graphene.

Inserting these distances in the relation for the Bragg angle (3.26) and relating the results with the measured distances in the diffraction patterns gives the scale of the images in rad/px.

From the spot angles found above and the calculated scale, an image with labelled disks of a desired Bragg disk radius can be constructed. The radius of the disks was set to be slightly smaller than the convergence angle found from the mean diffraction pattern, to minimise effects from non-overlapping parts of the disks. This label image is shown in Fig. 3.21 c). For better results the data is binned by a factor of two before fitting by averaging always four adjacent diffraction patterns.

The steps described above have to be done only once for each data set.

To analyse a diffraction pattern corresponding to a specific position, first the mean diffraction pattern is subtracted from the selected one to minimise effects of the central disk, then each of the outer Bragg disks is selected and fitted separately to a cosine function of the form

$$f(\mathbf{x}) = A \cos\left(2\pi \, \nu \, \hat{\mathbf{n}} \cdot \mathbf{x} + \phi\right), \tag{3.27}$$

where the unit vector $\hat{\mathbf{n}}$ is given by

$$\hat{\mathbf{n}} = \begin{pmatrix} \cos \theta_{prop} \\ \sin \theta_{prop} \end{pmatrix}. \tag{3.28}$$

The fitting parameters are therefore the amplitude A, the frequency ν, the propagation angle θ_{prop} and the phase shift ϕ.

In Figure 3.23 the process is shown for one example position of the simulated dataset. The six disks of the diffraction pattern are selected and fitted. For the experimental dataset a slight Gaussian filter is applied before fitting.

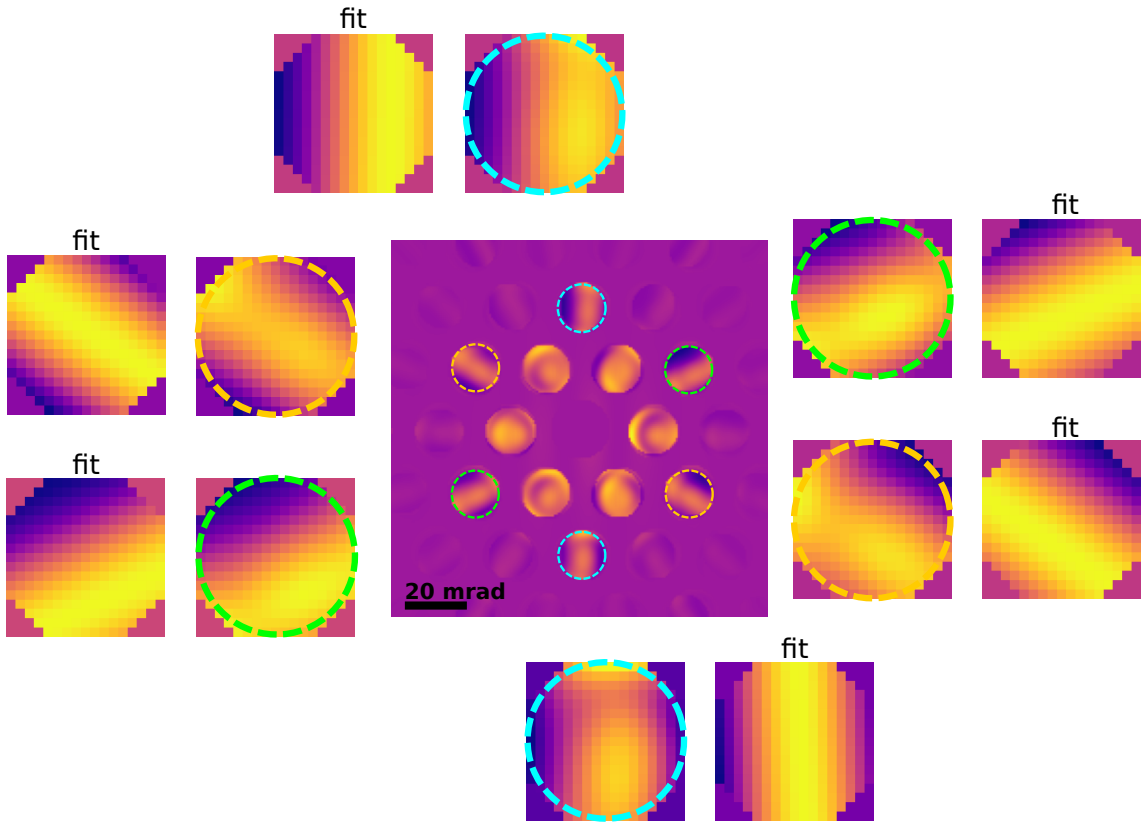

Figure 3.23: An example diffraction pattern with the disks used for fitting marked by differently coloured circles and shown higher magnified next to the pattern. The cosine fits are shown next to the corresponding disks.

The fitting was performed using the scipy native routine curve_fit iteratively starting with three pre-set starting conditions and generating new starting conditions in a Monte Carlo type fashion until either 10 iterations have been reached, in which case the fit is considered a failure, or the r^2 value of the resulting fit is within a given range and the procedure is considered a success.

Once the cosine parameters are established, information regarding the interlayer distance and defocus can be calculated from the relations discussed above and the relation of the frequency and wavelength

$$\nu = 2\pi\,\lambda. \tag{3.29}$$

To get the more relevant fringe wavelength in angular units θ_λ, the calculated fringe wavelength λ in units of pixels is multiplied by the calculated scale. The interlayer distance and defocus are calculated for every position of the map as discussed above.

In addition to determining the value for every position, also separate regions corresponding to AA and AB stacking orders were chosen and the diffraction patterns averaged before fitting.

Theoretically also the real space positions of the atoms can be extracted from the interference fringes through the structure factor, giving information about lattice distortion. However as the focus of this work was on the 3D structure of the bilayer samples this line of analysis was not further pursued.

3.6.4 Reconstruction of virtual images

Although the maps were recorded with a defocused probe, a virtual ADF image with an inner radius of 35 mrad and an outer radius of ~ 50 mrad was reconstructed from the data using the python package py4DSTEM. The outer radius was chosen as the maximum possible with the recorded diffraction pattern size.

By comparing the real MAADF image recorded at the position of the map and the reconstructed image, the influence of drift can be seen and the AA and AB regions can be selected more accurately.

3.6.5 DFT calculations

The DFT relaxed structure file of 3.15° twisted bilayer graphene was taken from Ref. [5] and is freely available. The calculation parameters are also detailed there.

3.6.6 Image simulations

Image simulations were done using the package *ab*TEM [60], developed by Jacob Madsen and Toma Susi, as well as the atomic simulation environment [61]. A potential was calculated using the independent atom model with 1024 grid points and the sampling over the scan area was done with slightly better than Nyquist sampling. The convergence angle was set at 31 mrad and the detector was constructed with an inner radius of 60 and an outer radius of 80 mrad. For

post-processing a slight interpolation was used and some Poisson noise was applied.

3.6.7 Defocused 4D-STEM simulations

The simulations were based on the freely available 4D-STEM simulations from Ref. [5]. A potential was again calculated using the independent atom model with 1024 grid points and slightly better than Nyquist sampling was used. The convergence angle was set at 8 mrad and the pixelated detector was constructed to have a maximum angular range of 50 mrad.

Chapter 4

Results and discussion

4.1 Effect of the laser for cleaning and fabrication of bilayer graphene

This first section gives an overview over the effect laser treatment has on monolayer graphene samples. The data collected is very limited, as the focus of this work was the interferometric measurements discussed below.

4.1.1 Cleaning effect

The most prominent effect of the laser treatment is its impact on sample cleanness. While for untreated samples the majority of the sample area is covered with amorphous contamination as can be seen in Fig. 4.1 a), heating with laser irradiation leads to the formation of large clean sample areas as shown in Fig. 4.1 b). Here this effect was not studied in detail but solely used as means to an end because large clean areas are needed for proper analysis of small angle moiré patterns.

4.1.2 Creation of folds

As discussed above, the heating of graphene leads to a contraction of the material due to the negative thermal expansion coefficient. This effect was successfully used for the fabrication of twisted bilayer graphene samples.

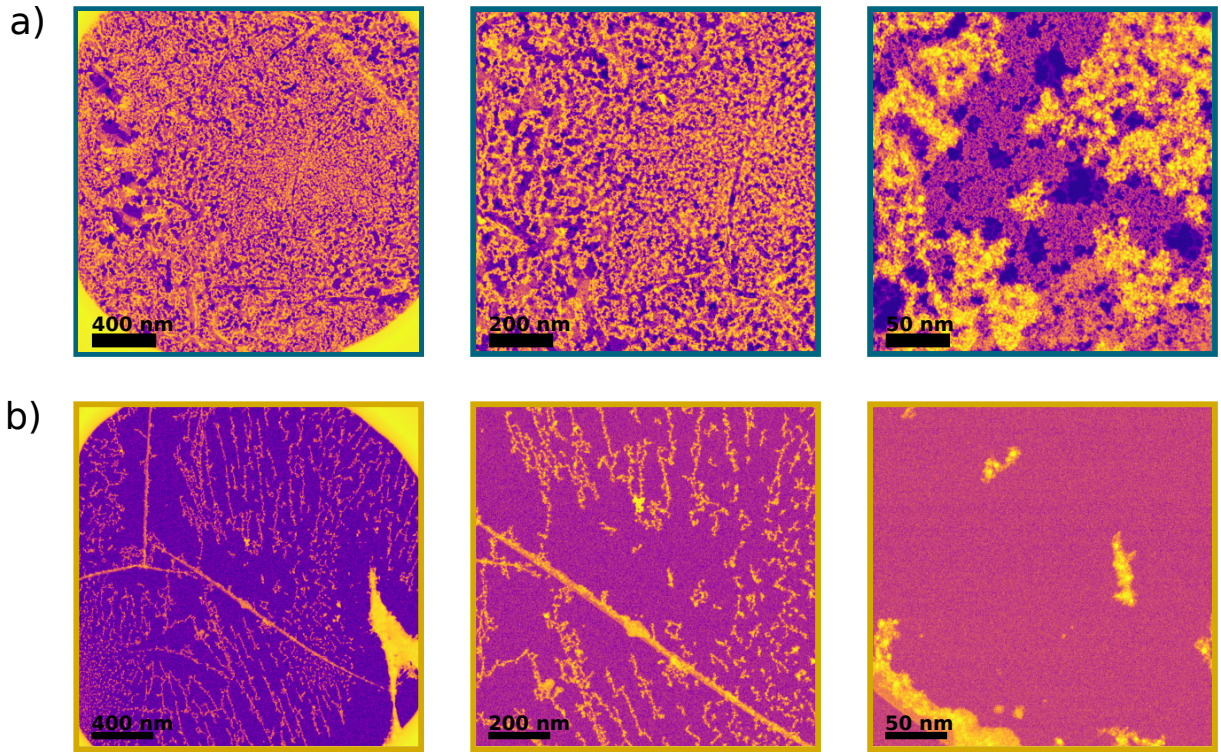

Figure 4.1: STEM-MAADF images showing a comparison of a non-cleaned sample (panel a) and a cleaned sample region (panel b) in three different magnifications. The bright contrast indicates contaminated regions.

The contraction of the layers results in the formation of folds where three layers are stacked. In addition to these trilayers, often narrow bilayer areas can be found at one edge of these folds. This is attributed to ripping of the layer in the folding process as can be seen schematically in Fig. 4.2 a). The panel b) of Fig. 4.2 shows the stacking sequence of mono- to bi- to trilayer graphene.

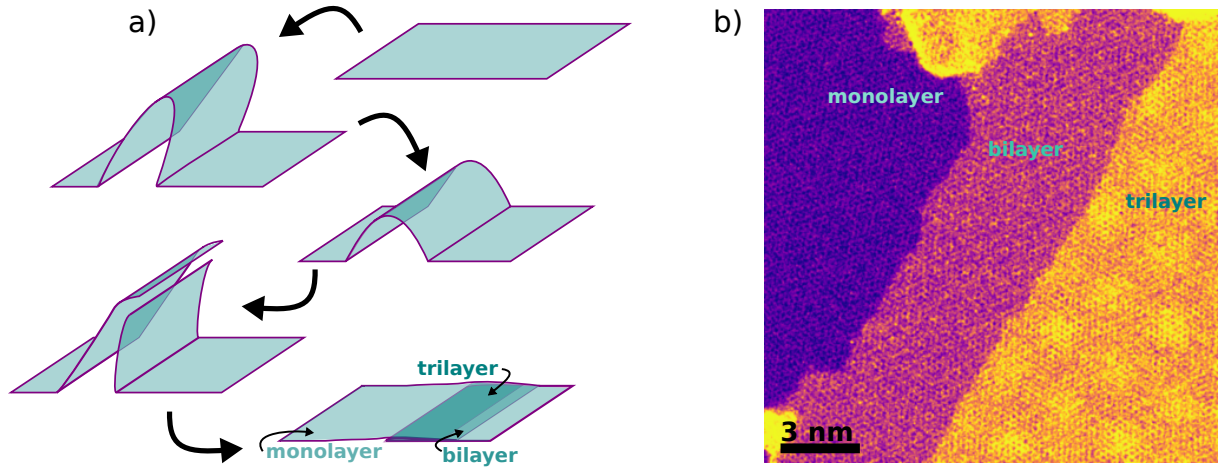

Figure 4.2: a) Schematic illustration of the layer folding process. b) STEM-MAADF image of a monolayer/bilayer/trilayer transition.

The extent and shape of these folds differed qualitatively for the two laser powers used. However, also different samples showed different fold characteristics, which could be linked to the shadowing of the laser, as well as to structural differences inherent to the samples.

Angular range of formed bilayers

The bilayer regions showed various characteristics. Often only narrow regions next to the folds showed bilayer stacking as discussed above. However, especially for higher laser power, the folds often spanned many hundred nanometers, and various twist angles could be found even within one region.

An example of such a fold is shown in Fig. 4.3. Here a change of the moiré patterns is clearly visible over the range of the sample, especially in the pockets between contamination agglomerations. As discussed in section 2.1.4 this is connected to a change in twist angle.

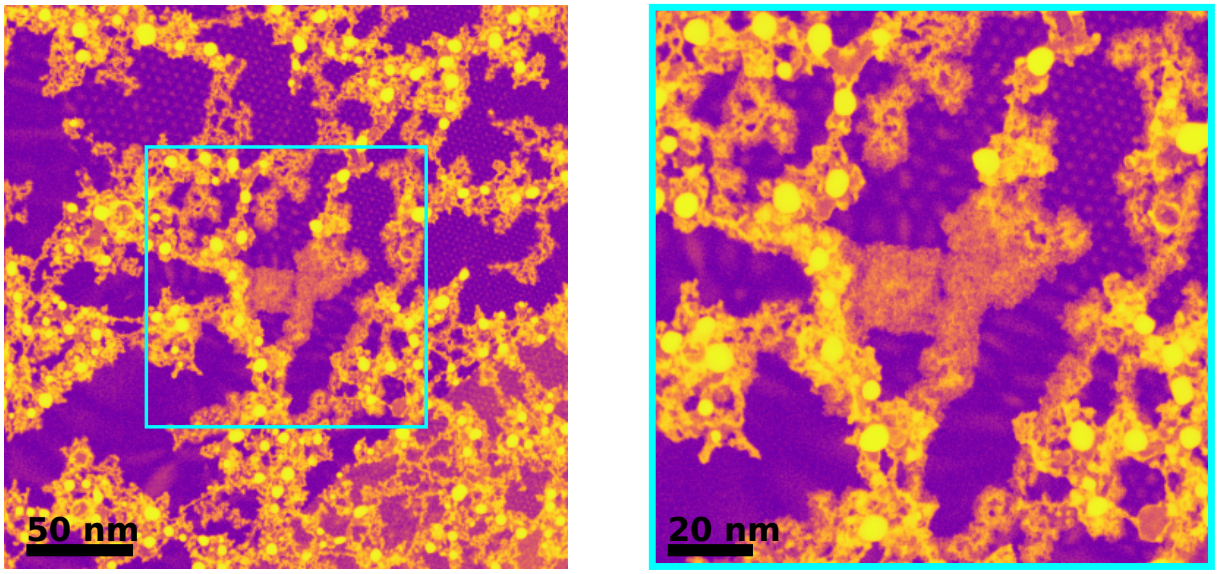

Figure 4.3: STEM-MAADF images showing an example sample region consisting of mostly bilayer graphene that shows different twist angles as apparent from the moiré features.

Another feature visible in this figure ise the wavelike structure seen on the left hand side of the image, where the moiré spots are not round but show elliptical character. The formation of such elliptical moiré patterns has been reported for structures where small twist angles are combined with lattice strain [62]. Here these features are attributed to a combination of the effect of strain introduced by heating and folding and a small, non-constant twist angle.

The square of higher contrast in the centre of the image is due to the pinning of contamination by the electron beam.

Various bilayer graphene regions have been found, exhibiting a wide range of different twist angles with the larger ones around 10°. The smallest angles where a wide enough continuous moiré pattern could be found were between 2° and 3°. A few moiré patterns are shown in Fig. 4.4. Their angles were analysed as discussed in section 3.6.2 using the Fourier transformation. The cell sizes of the resulting patterns can be calculated from the twist angles using equation 2.3.

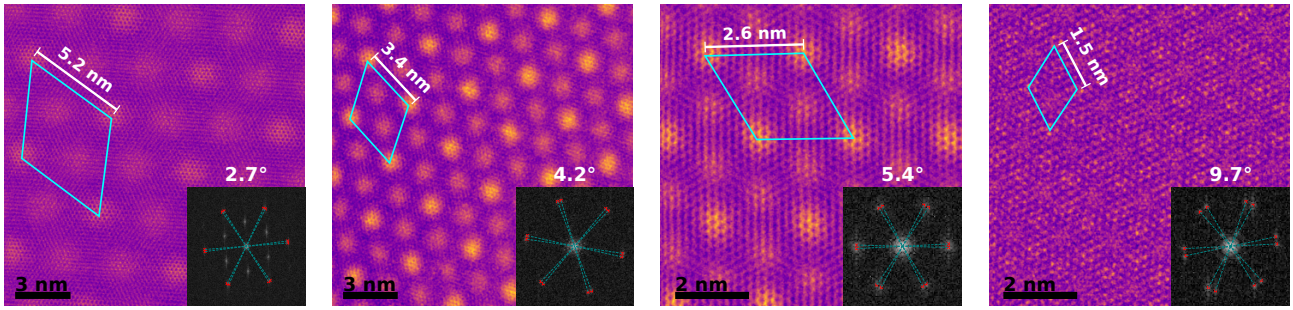

Figure 4.4: STEM-MAADF images showing an overview over different encountered moiré patters with the moiré cells indicated in blue. The insets correspond to the power spectra of the Fourier transformed images that were used to calculate the twist angles. The Fourier spots used for analysis are marked in red and blue lines connect the symmetric spots.

4.2 Analysis of interferometric 4D-STEM data

4.2.1 Simulated dataset

Image reconstruction

A virtual ADF image was reconstructed with an angular range of 35 to 60 mrad and is shown next to a simulated MAADF image of the same field of view in Fig. 4.5.

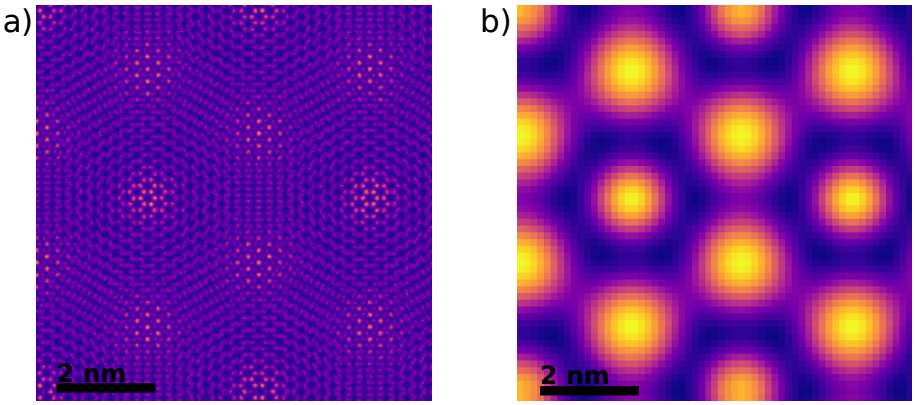

Figure 4.5: a) Simulated STEM-MAADF image of 3.15° twisted bilayer graphene. b) Virtual ADF image reconstructed from defocused 4D-STEM simulations.

Even though no good resolution can be achieved in the reconstruction because of the defocused nature of the measurements, the moiré pattern can be discerned, making the reconstructed image a valuable tool for orientation in the 4D-STEM datacube. This is especially important in experimental measurements where no MAADF image can be recorded simultaneously with the defocused map.

Fit parameters

The interference features were analysed for every position of the binned dataset, fitting each diffraction disk separately. This results in six maps each for the amplitude, phase shift, fringe rotation and fringe wavelength (calculated from the fringe frequency) that can be averaged to give a mean fitting parameter for ever position. Fits that did not converge or resulted in rotation values over 8° were excluded from the maps to show the features more clearly. The maps of the fitted fringe wavelength and fringe rotation are shown in Fig. 4.6, the phase shift and amplitude can be seen in Fig. 4.7.

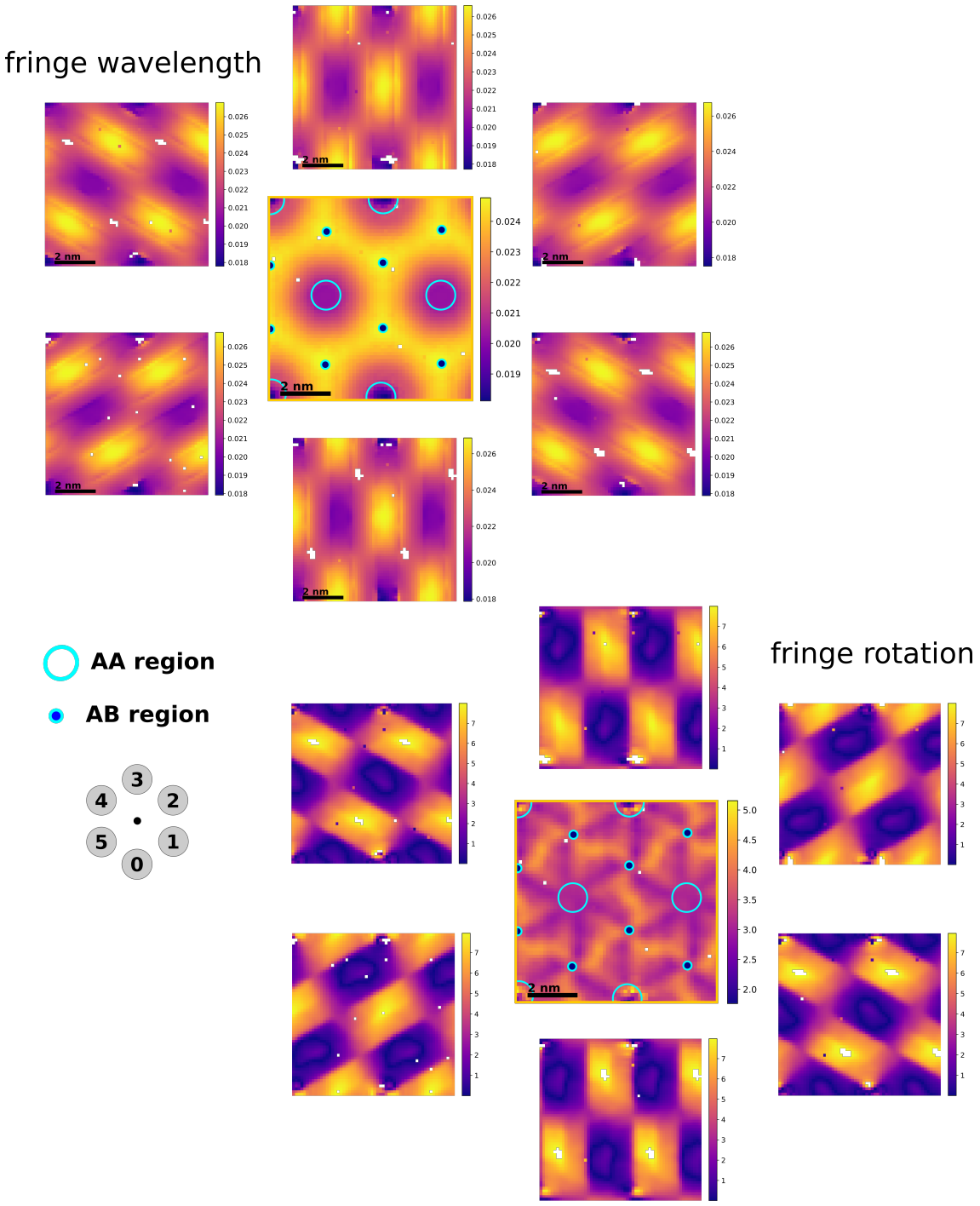

Figure 4.6: Maps for the fitted fringe wavelength (m) and fringe rotation (°) of the interference features. For each parameter the results for the separate diffraction disks are arranged around the averaged map in the order shown in the diagram on the left. The AA and AB stacking regions are marked in the averaged maps by blue circles and blue dots, respectively. The white pixels correspond to positions where the fit did not converge or the rotation angle was larger than 8°.

This analysis shows a clear dependence of the interference features on the diffraction direction. While opposite scattering disks show similar behaviour, the features of the three independent scattering directions are rotated by 60° around the AA positions. Averaging the fit results of the

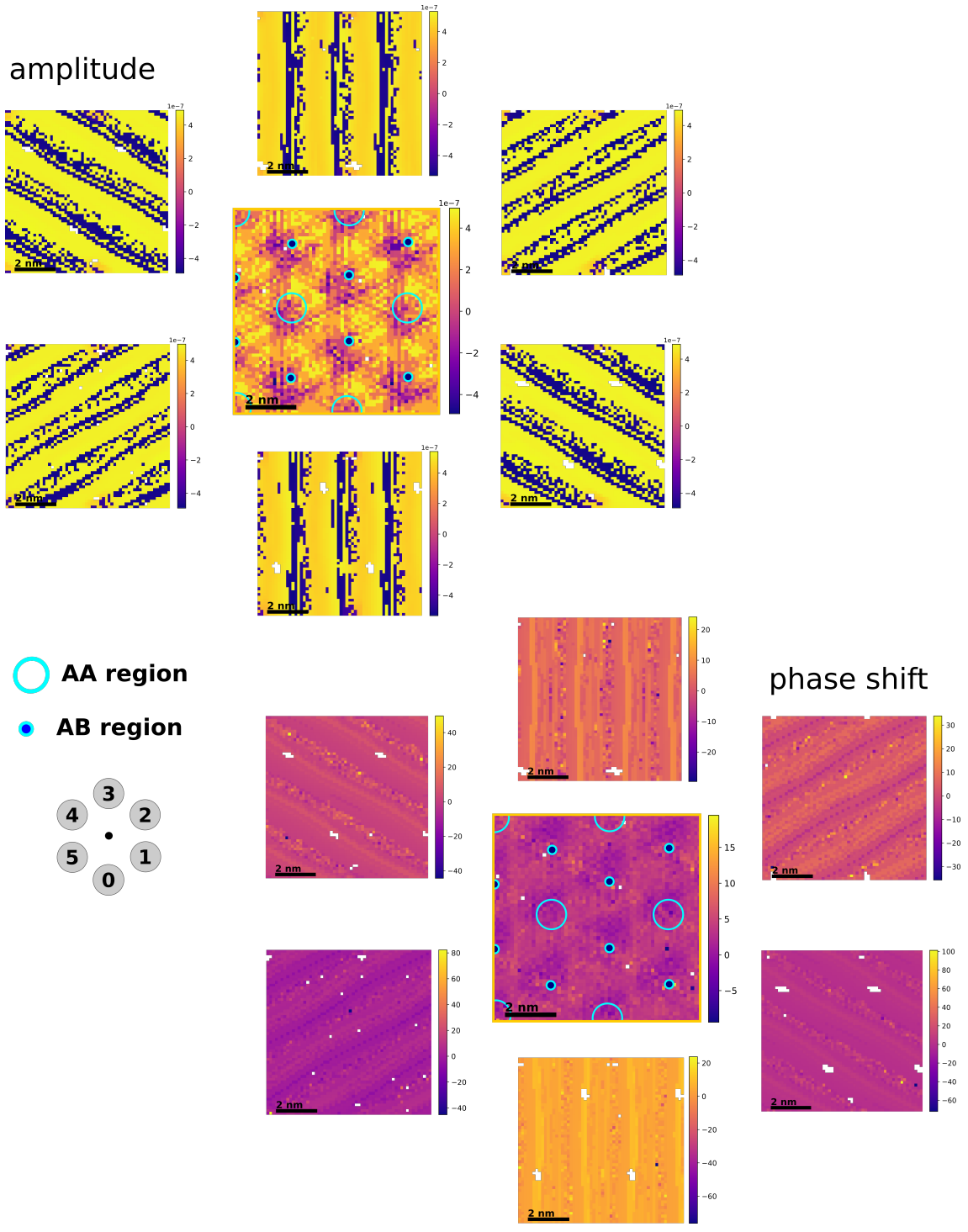

Figure 4.7: Maps for the fitted amplitude (grey value) and phase shift (rad) of the interference features. For each parameter the results for the separate diffraction disks are arranged around the averaged map in the order shown in the diagram on the left. The AA and AB stacking regions are marked in the averaged maps by blue circles and blue dots, respectively. The white pixels correspond to positions where the fit did not converge or the rotation angle was larger than 8°.

six different disks gives maps that show a clear connection to the moiré pattern of the simulated graphene structure.

Interlayer distance analysis

From the fitted fringe wavelength and fringe rotation values the interlayer distance can be calculated for every sample position. The interlayer distance maps resulting from the six separate diffraction disks are shown in Fig. 4.8.

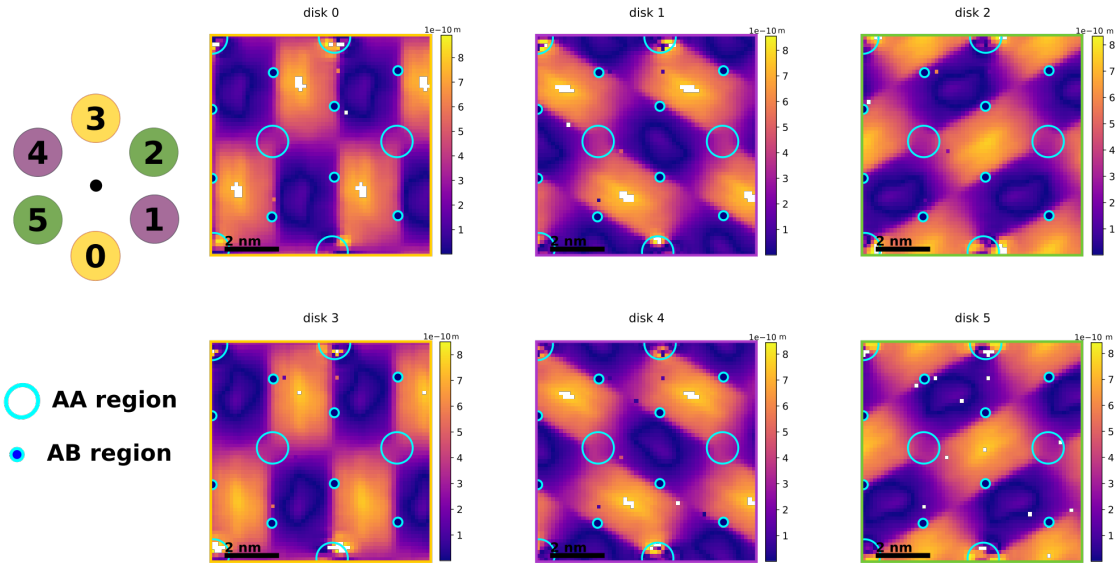

Figure 4.8: Interlayer distance maps for each diffraction disk. The positions of the disks in the diffraction pattern are shown schematically in the diagram on the left of the figure. AA and AB stacking regions are marked with blue circles and blue disks, respectively. The white pixels correspond to positions where the fit did not converge or the rotation angle was larger than 8°.

As already for the fitting parameter, also here the direction dependence of the calculated features can be clearly seen. The calculated values range from close to 0 to approximately 8 Å with the maxima and minima located in the transition regions between AA and AB stacking regions. Interestingly, because of the apparent rotation of the features by an angle of 60° around the AA regions, every maximum position of one disk corresponds to a minimum position of a different disk. Therefore, when the maps are averaged, the maxima and minima become less pronounced and the range of the interlayer distances decreases. Also the pattern becomes symmetric and the moiré features can be recognised. In Fig. 4.9 a histogram and map of the averaged interlayer distance values are shown and compared to the expected interlayer distance calculated directly from the coordinates of the simulated structure.

While the moiré pattern can be recognised from the averaged interlayer distance map, the overall behaviour of the structure is not reproduced. The mean interlayer distance calculated from the averaged values is 3.29 ± 0.33 Å, which agrees well with the expected value of 3.29 Å but has a

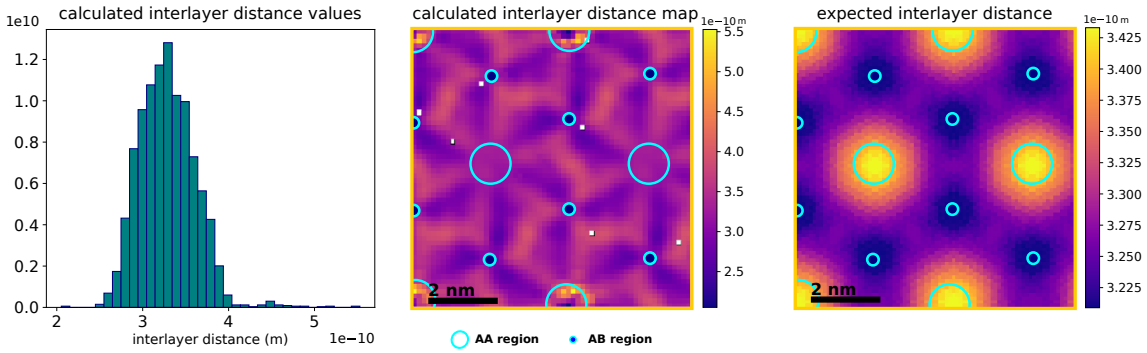

Figure 4.9: Comparison of the interlayer distance calculated from the interference features and the expected interlayer distance calculated directly from the coordinates of the simulated structure. The high variation of the interlayer distances calculated from the interference features is clearly shown in the histogram.

very high uncertainty due to the large variation of the values for the different diffraction disks at each position.

Defocus analysis

Similar to the interlayer distance discussed above, the defocus was calculated separately for every diffraction disk resulting in the maps shown in Fig. 4.10.

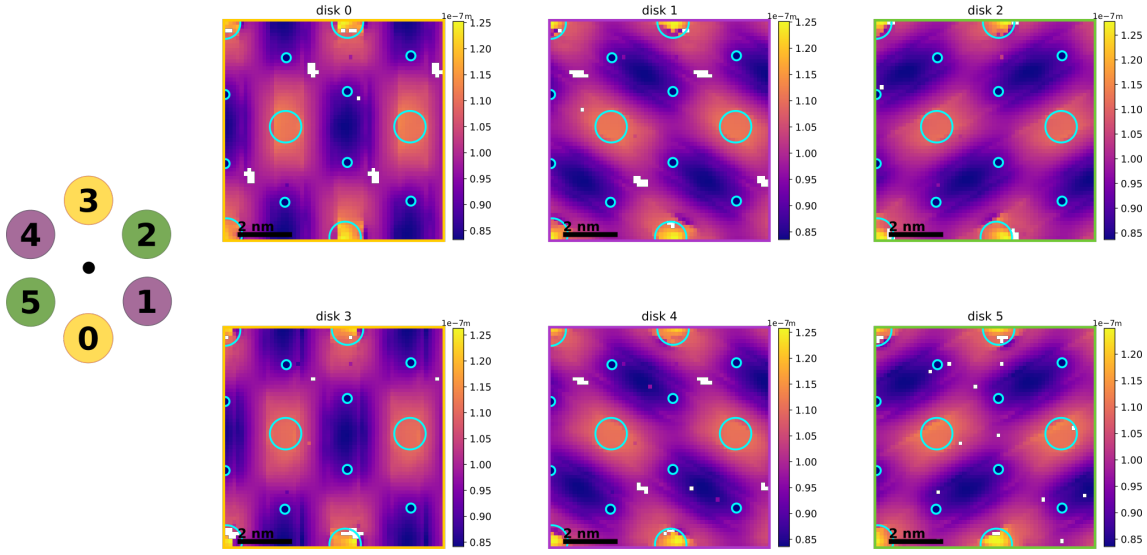

Figure 4.10: Defocus maps for each diffraction disk. The positions of the disks in the diffraction pattern are shown schematically in the diagram on the left of the figure. AA and AB stacking regions are marked with blue circles and blue disks, respectively. The white pixels correspond to positions where the fit did not converge or the rotation angle was larger than 8°.

Like the interlayer distance, also the defocus inherits the directional dependence from the fitted parameters. If the maps for the different disks are averaged, the resulting defocus map shows hexagonal symmetry and the connection to the moiré pattern is evident. Maps of the averaged defocus as well as the expected defocus variation calculated directly from the coordinates are shown in Fig. 4.11.

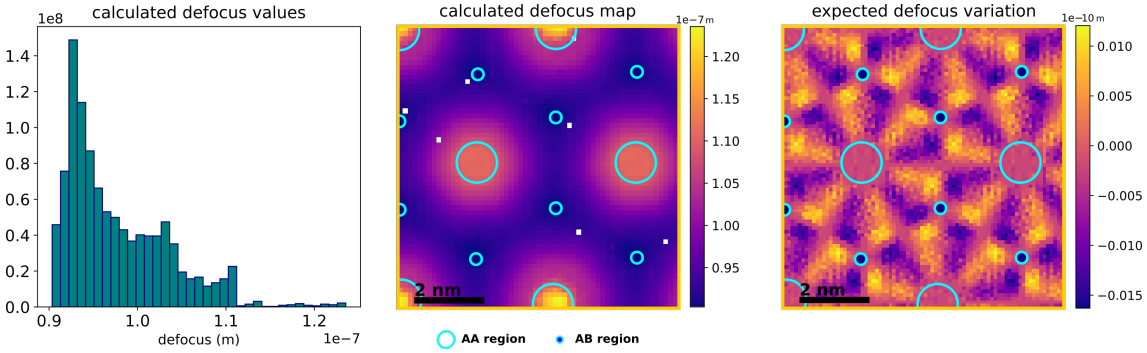

Figure 4.11: Comparison of the defocus calculated from the interference features and the expected defocus variation calculated directly from the coordinates of the simulated structure. The order of magnitude of the mean defocus is correct, however, the variation is in the order of 10 nm instead of the expected fractions of Ångstöm.

The mean defocus calculated from the map is 978 ± 58 Å, which agrees relatively well with the value of 1000 Å used in the simulation. However, the variation does not agree with the expected features, and is drastically too high, with values in the order of 10 nm instead of the expected fractions of Ångstöm.

Structure determination from the interference fringes

As seen above, the moiré pattern can clearly be recognised from the analysis of the interference features due to their direction dependence. From the averaged feature maps AA and AB stacking regions can be identified because of their role as centres of symmetry for the rotation of the features for the different diffraction disks. Due to this, also the variation of the values calculated for the six disks at every position is a good indicator of the structure. Because of the high symmetry nature of the AA and AB stacking regions, the variation of the features there is minimal. Fig. 4.12 shows the comparison of the averaged interlayer distance map and the standard deviation of the interlayer distances of the different disks with the simulated STEM-MAADF image.

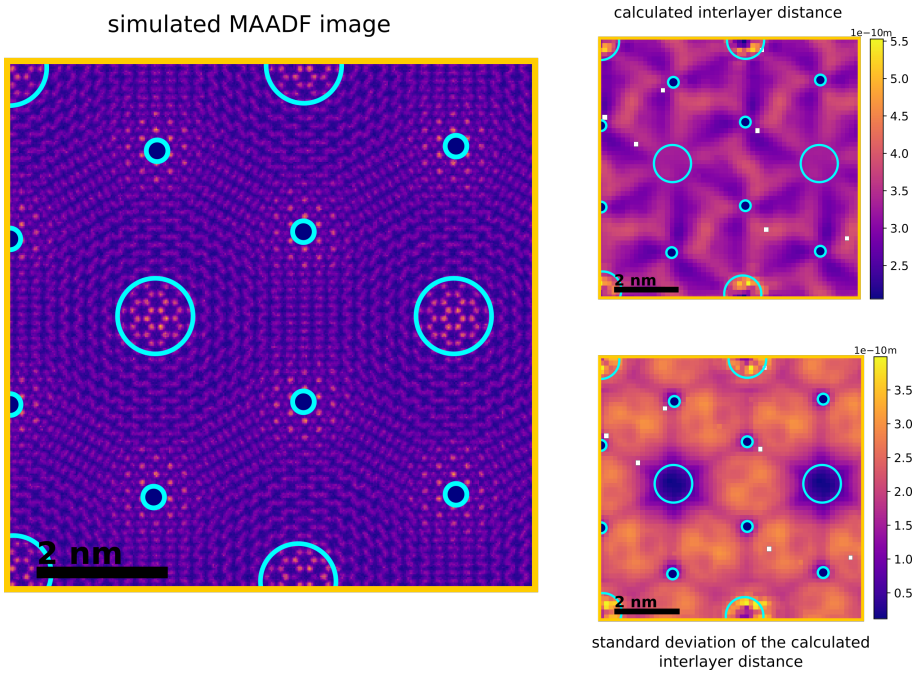

Figure 4.12: Comparison of the simulated STEM MAADF image with the maps for the averaged interlayer distance and the standard deviation of the interlayer distances calculated for the different disks at each position. Especially for the latter, the moiré structure can clearly be determined.

AA and AB stacking regions

To analyse the dependence of the interlayer distance on the stacking order, two AA regions and four AB regions of the simulated structure were chosen and the interlayer distances were calculated from the averaged diffraction patterns. The chosen AA and AB stacking regions and the averaged diffraction patterns are shown in Fig. 4.13.

The calculated interlayer distance values for the six diffraction disks of the averaged AA and AB diffraction patterns are listed in table 4.1.

While the Gaussian error analysis of the distances for each disk give low uncertainties, the results for the different disks vary widely. Overall the interlayer distance calculated for AA stacking is higher than for AB stacking. The lower uncertainties calculated for the AB region are attributed to the averaging over four patterns compared to two for the AA stacking regions. Averaging over all disks gives an interlayer distance of 3.42 ± 0.17 Å for the AA regions, and an interlayer distance of 3.091 ± 0.043 Å for the AB regions. While the value for the AA interlayer distance calculated this way agrees well with the expected value of 3.43 Å, the AB interlayer distance is significantly smaller than the expected 3.21 Å.

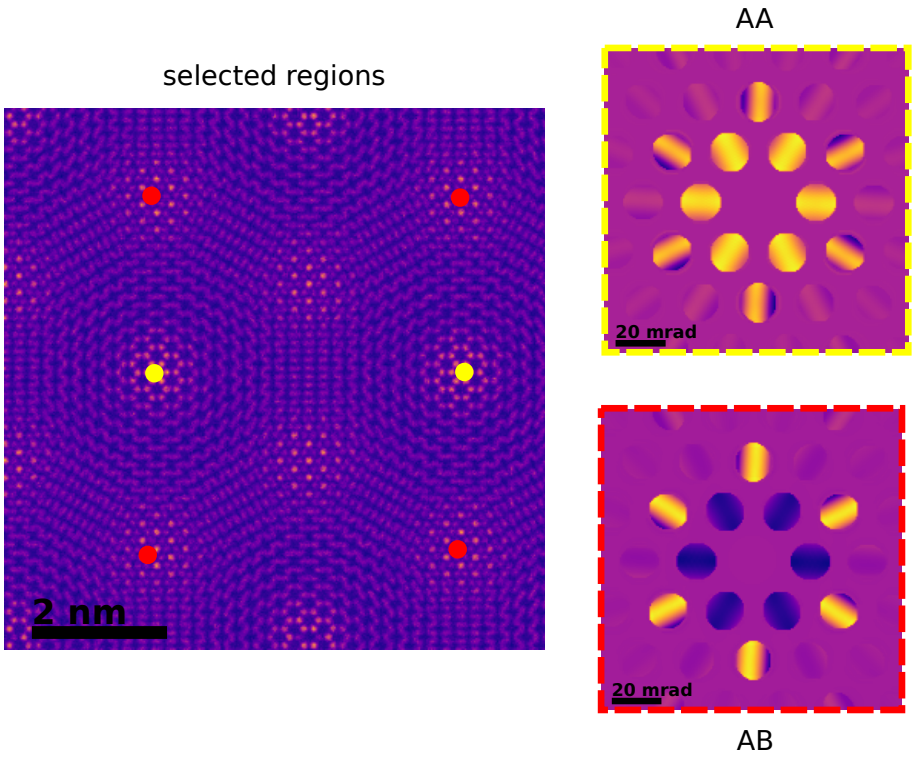

Figure 4.13: Two positions of AA stacked regions and four positions of AB stacked regions indicated with yellow and red dots respectively on the simulated STEM MAADF image on the left hand side. Diffraction patterns corresponding to these positions were selected for analysis of the interlayer distance. The averaged diffraction patterns are shown on the right hand side framed in yellow and red.

	interlayer distance AA region (Å)	interlayer distance AB region (Å)
disk 0	3.40 ± 0.12	3.105 ± 0.035
disk 1	3.44 ± 0.11	3.032 ± 0.037
disk 2	3.044 ± 0.099	3.064 ± 0.037
disk 3	–	3.099 ± 0.037
disk 4	3.28 ± 0.11	–
disk 5	3.06 ± 0.11	3.158 ± 0.038

Table 4.1: Interlayer distance calculated for the six diffraction disks of the averaged AA and AB patterns. The uncertainties were calculated using Gaussian error propagation. For the disks where no value is given, the fits did not converge.

4.2.2 Experimental dataset

Experimental data was collected and analysed for a region of a sample lasered at 42% power. An overview over the sample position is presented in Fig. 4.14. The twist angle of the bilayer

graphene in this region was measured to be $4.2 \pm 0.2°$, where the uncertainty was assumed as the standard deviation of the six symmetric angles between the Fourier spots.

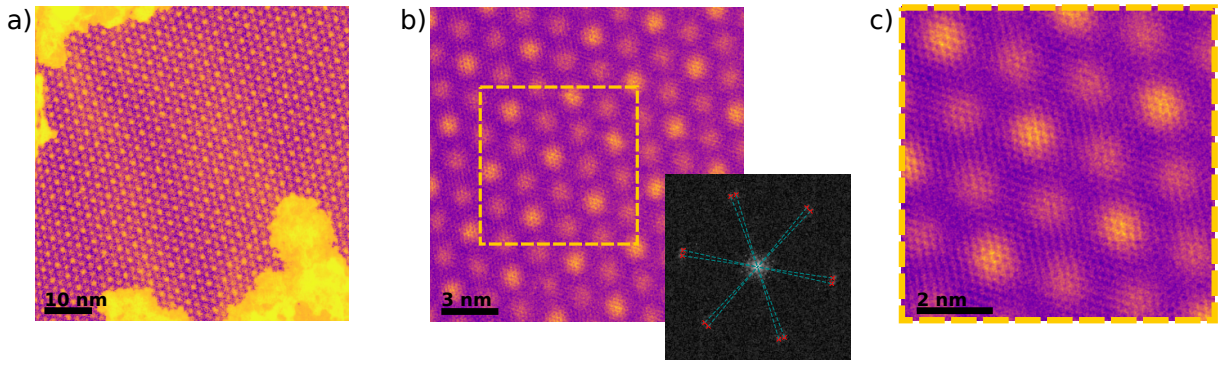

Figure 4.14: a) and b) Different magnification STEM-MAADF images of the analysed bilayer sample region. The inset shows the power spectrum of the Fourier transformed image used for determination of the twist angle. c) STEM-MAADF image recorded at the same position as the 4D-STEM map. This region is indicated in panel b) by a yellow square.

The mean diffraction pattern, as well as the pattern for a single example position of the dataset are shown in Fig. 4.15.

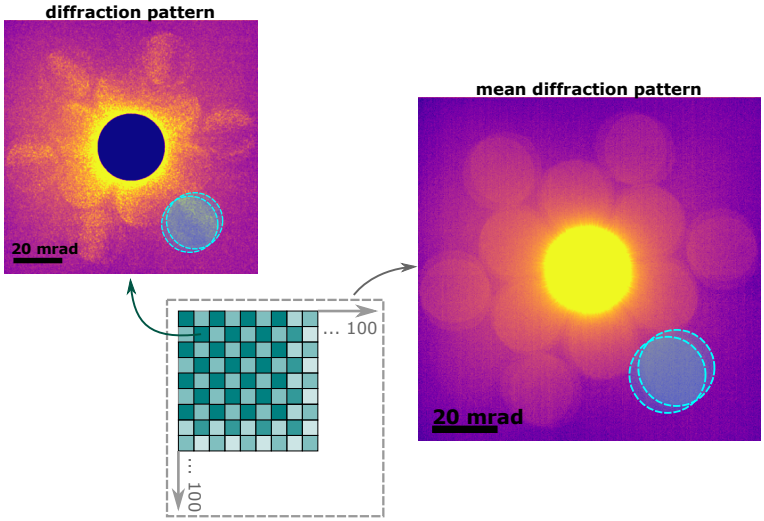

Figure 4.15: One example diffraction pattern with a masked central spot and the mean diffraction pattern of the whole area. The blue circles indicate the overlapping diffraction disks originating from the two layers.

Image reconstruction

In Fig. 4.16 the reconstructed ADF and the recorded MAADF image are shown in panel a) and b). In panel c) the two images are overlayed and the real image is distorted to match the

drift present while imaging. The drift was roughly quantized to 0.05 Å/line and 0.01 Å/line in x and y direction respectively. However, due to the change of probe settings needed for recording defocused maps, the scanned region is not identical to the region shown in the MAADF image, which makes identifying the features of the image difficult. Here the focus is more on identifying the AA and AB regions than on finding the exact relation of the images.

The strong influence of drift stems from the long acquisition times needed for recording the 4D-STEM data. For direct electron detectors, the recording of the maps takes less time and the effects of drift are minimised.

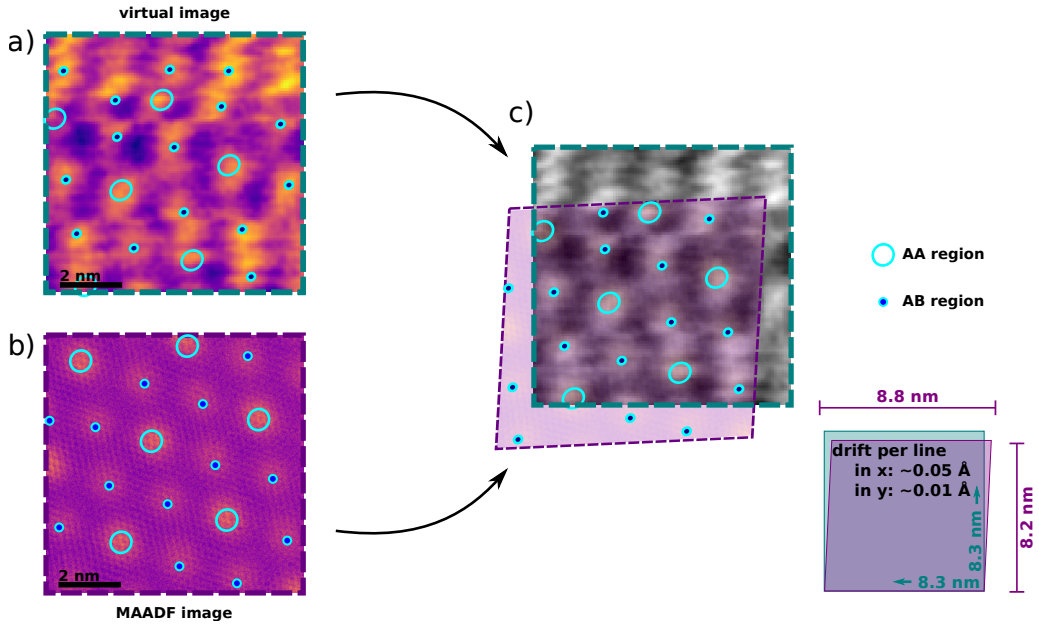

Figure 4.16: Comparison of a virtual image reconstructed from the defocused 4D-STEM map with a STEM-MAADF image of approximately the same region. a) Reconstructed ADF image. b) STEM-MAADF image. c) Overlayed images are used to give an approximate quantisation of the drift present while recording the map. The AA and AB regions are marked by blue circles and blue dots respectively.

Fit parameters

All diffraction disks were fitted separately for every second position of the map. Even though the data was binned by a factor of 2, many fits did not succeed and the resulting maps are difficult to interpret. Maps of the separately fitted disks, as well as the maps averaged over the six diffraction disks are shown in Fig. 4.17.

While the patterns do show different behaviour depending on the disk, other than before they

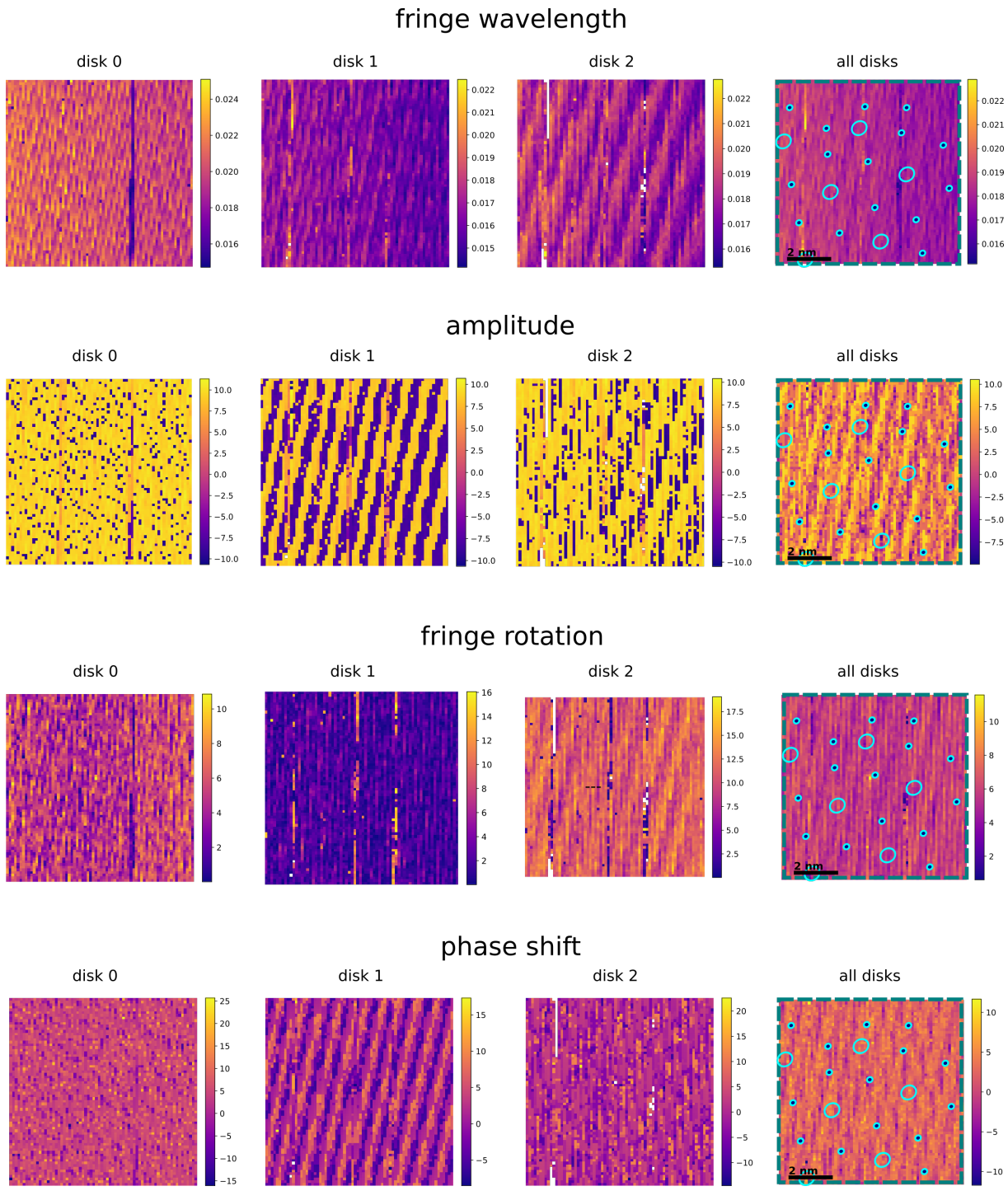

Figure 4.17: Maps for the fitted fringe wavelength (m), amplitude (grey value), fringe rotation (°) and phase shift (rad) of the interference features. Because the opposite disks show similar behaviour, only the results for the first three disks and the averaged fit parameters are shown. The AA and AB stacking regions estimated above are marked in the averaged maps by blue circles and blue dots, respectively. The white pixels correspond to positions where the fit did not converge.

offer no clear correspondence to the moiré pattern. The line-like features evident in almost all maps are not recognisably connected to the structure.

Interlayer distance and defocus analysis

The interlayer distance and defocus was also calculated for ever probe position, however, suggested by the maps of the fitting parameters above, the values offer no clear correspondence to the moiré structure and no clear minima and maxima as seen in the simulations. Fig. 4.18 shows the mean interlayer distance and defocus array plot, as well as the standard deviation of the interlayer distance calculated from the different disks for every position. The average interlayer distance was calculated to 6.7 ± 1.2 Å and the average defocus is 928 ± 35 Å.

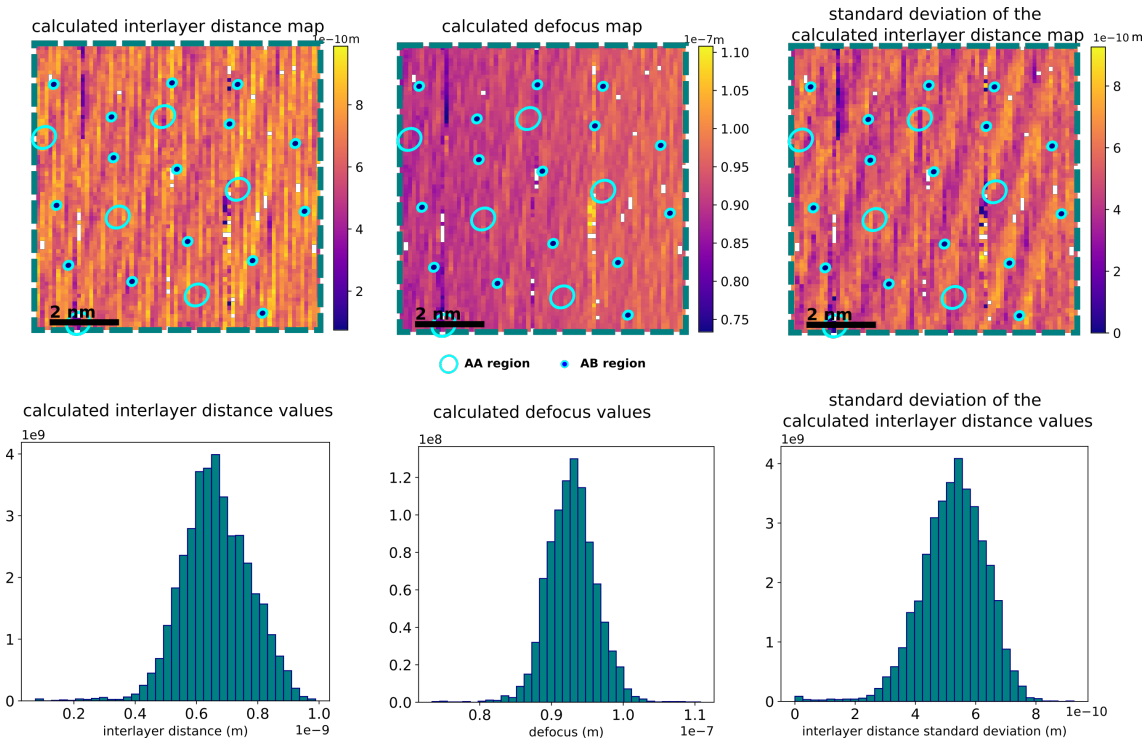

Figure 4.18: The averaged results for the interlayer distance, the defocus and the standard deviation of the interlayer distance calculated for every diffraction disk of one position. Blue circles and blue dots mark the estimated positions of AA and AB regions. The white pixels correspond to positions where the fit did not converge.

4.3 Discussion

There have been various studies on the interlayer distance depending on the different region of the moiré pattern. In 2014 Uchida et al. published a very detailed paper on the atomic corrugation due to moiré patterns where they used DFT calculations with a local-density approximation to simulate 58 commensurate tBLG structures and found a strong dependence of the interlayer distance on the twist and stacking order. For large twist angles, the structures show little corrugation and the interlayer distance has an almost constant value of 3.42 Å. When the twist angle gets smaller and a moiré pattern forms, a difference of the interlayer distances of AA and AB stacked regions emerges. The largest interlayer distance was found in the AA stacking regions, for AB stacking the layers are closest together. This corrugation, so the difference between the farthest and closest distance, gets more pronounced the smaller the twist angle becomes. While for an angle of 8.26° they found a corrugation of 0.07 Å, for 3.89°, the corrugation was already 0.12 Å [4].

While the analysis of the simulated data gave a reasonably good result for the mean interlayer distance as well as the average defocus, the behaviour of both properties with respect to the moiré pattern could not be reproduced. Another apparent problem is presented by the calculated defocus map. As mentioned before, the calculated mean defocus value reproduces the expected defocus within uncertainty limits, however, the variation of the defoucus calculated by the method is in the range of tens of nanometers, instead of the expected fractions of Ångström. Interestingly, the averaged interlayer distance map shown in Fig. 4.9, shows features that closely resemble the expected defocus variation, and vise versa, the averaged defocus map shown in Fig. 4.11 resembles the features expected for the interlayer distance. The diffraction direction dependence of all fitted parameters, is assumed to be an intrinsic effect of the defocused interference patterns that should be studied in more detail and cannot be explained by the simple model the analysis is based on at this state.

For the experimental data, the method produced little usable results. This is attributed to a combination of the drift, that makes connecting the recorded map to the real structure difficult, and the high noise level of the measurements. Both of these effects can be reduced by using a fast electron detector with a higher acquisition speed and better signal-to-noise ratio. In the current setup, the effect of drift can be reduced by lowering the acquisition time by, for example, reducing the number of recorded pixels. The signal-to-noise ratio can be increased by using a lower defocus value for the experiment, however, this results in smaller diffraction disks which can also be problematic for the analysis. The mean interlayer distance of 6.7 ± 1.2 Å calculated

from the recorded data, is almost twice the expected value for tBLG. This could be an effect of the sample preparation, as the bilayer regions are produced in the folding process by effectively stacking a third layer on top of a monolayer/bilayer transition as illustrated in Fig. 4.2 a). Due to this, for narrow folds, the bilayer graphene regions could be separated by more than the relaxed layer distance. Another possible cause for the higher interlayer distance is strain introduced by the heating process. However, as the method has not proven to be very reliable at its current state, the deviation from expected values does not necessarily have physical roots. Interestingly, even though the calculated maps do not show the diffraction direction dependency exhibited by interference features of the simulated dataset, there are line-like features in all fit parameter maps that do not depend on the scattering direction.

One method that was used in Ref. [5] to reduce the noise in the measurements, was the averaging of opposite diffraction disks, that were assumed to be symmetric. However as illustrated in 4.19 for an example of a simulated diffraction pattern, the opposite diffraction disks can show different interference features, which, if the disks are averaged, leads to an effective blurring of the fringes, therefore resulting in a higher fringe wavelength and less accurate fringe angle.

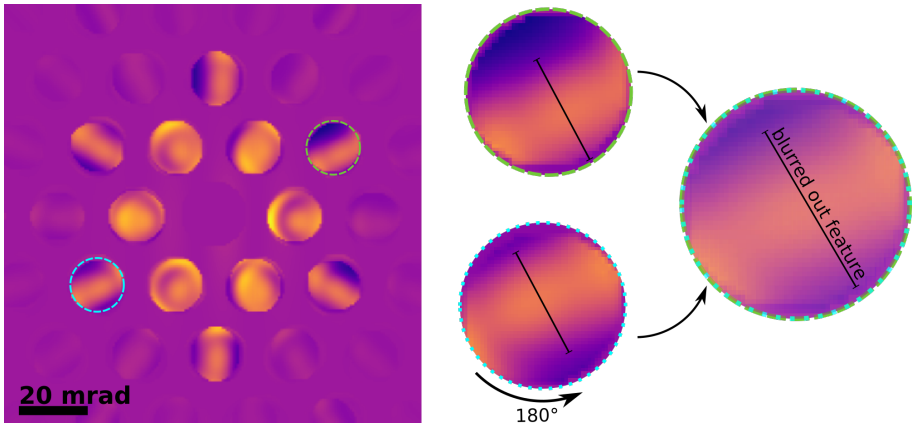

Figure 4.19: The averaging of two opposite diffraction disks of an example diffraction pattern marked with yellow and green circles leads to a blurring out of the interference features as shown by the overlay of both disks. Before averaging one of the disks has to be rotated by 180°.

Because the method at its current state gives reasonable average values, only detailed analysis of the results exposes the issues, that, as apparent from the discussion above, are still numerous.

Chapter 5

Conclusions and outlook

The goal of this thesis was to establish a workflow for the analysis of the interlayer distance and defocus variation in tBLG samples using defocused 4D-STEM and test it on simulated data, as well as to apply it to a real dataset.

Python code was written to semi-automatically mask the defocused diffraction patterns for each scan position, extracting the overlapping diffraction disks originating from the two layers of the structure. A cosine function is then fitted to the interference fringes formed in these overlap regions and the interlayer distance as well as the defocus can be calculated from the fit parameters using purely geometric relationships.

A defocused 4D-STEM measurement was simulated using a DFT relaxed tBLG structure with a twist angle of 3.15° and used to test the method. While the mean interlayer distance was calculated correctly, the behaviour of the interlayer distance with respect to structure variations could not be reproduced. Also for the defocus determination only the mean value could be correctly established. The method revealed an interesting dependence of the interference features on the scattering direction that leads to very high variations in the fit parameters calculated for the six different diffraction disks of each pattern. This effect is lowest for the AA and AB stacked regions of the moiré pattern formed by the tBLG, which makes it possible to determine the moiré structure from the interference features.

In addition to the simulated data, also experimental measurements were performed. To produce clean tBLG samples, CVD grown monolayer graphene on SiN grids was folded using the heating effect of laser irradiation under UHV conditions, a method not reported before. A defocused 4D-STEM dataset of a 4.2° tBLG region was recorded using the Nion UltraStem 100 microscope

and the interference features were analyse. Due to influences of drift and noise, only a mean interlayer distance and defocus value could be calculated. The mean interlayer distance is higher than expected for bilayer graphene, which could be a result of the sample preparation.

While the method did not produce the hoped-for results, important groundwork has been laid to continue exploring this line of research. Beside further testing and improving the method using simulations, also the experimental setup will be improved with the implementation of a direct electron detector in the near future, which will considerably reduce the problems of drift and noise. The long-term goal is to establish a robust and reliable method to gain information about the 3D structure of not only tBLG, but any twisted multilayer material – a goal that is very optimistic, yet not impossible.

Bibliography

[1] NBC-News. 'Kon-Tiki' raft re-creation gets fresh start. https://www.nbcnews.com/id/wbna9507963.

[2] Novoselov, K. S. *et al.* Electric Field Effect in Atomically Thin Carbon Films. *Science* **306**, 666–669 (2004). DOI: 10.1126/science.1102896.

[3] Hofer, C., Mustonen, K., Skakalova, V. & Pennycook, T. J. Picometer-precision few-tilt ptychotomography of 2D materials (2022). ArXiv:2108.04625 [cond-mat, physics:physics].

[4] Uchida, K., Furuya, S., Iwata, J.-I. & Oshiyama, A. Atomic corrugation and electron localization due to moiré patterns in twisted bilayer graphenes **90**, 155451. DOI: 10.1103/PhysRevB.90.155451.

[5] Zachman, M. J. *et al.* Interferometric 4D-STEM for Lattice Distortion and Interlayer Spacing Measurements of Bilayer and Trilayer 2D Materials. *Small* **17**, 2100388 (2021). DOI: 10.1002/smll.202100388.

[6] Urade, A. R., Lahiri, I. & Suresh, K. S. Graphene properties, synthesis and applications: A review **75**, 614–630. DOI: 10.1007/s11837-022-05505-8.

[7] Yang, G., Li, L., Lee, W. B. & Ng, M. C. Structure of graphene and its disorders: a review **19**, 613–648. DOI: 10.1080/14686996.2018.1494493.

[8] Avouris, P., Heinz, T. F. & Low, T. (eds.) *2D materials: properties and devices* (Cambridge University Press). OCLC: 992976138.

[9] Balandin, A. A. *et al.* Superior thermal conductivity of single-layer graphene **8**, 902–907. DOI: 10.1021/nl0731872.

[10] López-Polín, G. *et al.* Tailoring the thermal expansion of graphene via controlled defect creation **116**, 670–677. DOI: 10.1016/j.carbon.2017.02.021.

[11] M K, K. & Jaiswal, M. Graphene: A review of optical properties and photonic applications. *Asian Journal of Physics* **25**, 809–831 (2016).

[12] Papageorgiou, D. G., Kinloch, I. A. & Young, R. J. Mechanical properties of graphene and graphene-based nanocomposites. *Progress in Materials Science* **90**, 75–127 (2017). DOI: 10.1016/j.pmatsci.2017.07.004.

[13] Callister, W. D. & Rethwisch, D. G. *Materials science and engineering: an introduction* (John Wiley & Sons, Inc.), 10th edition edn. OCLC: 992798798.

[14] Gutiérrez-Cruz, A., Ruiz-Hernández, A. R., Vega-Clemente, J. F., Luna-Gazcón, D. G. & Campos-Delgado, J. A review of top-down and bottom-up synthesis methods for the production of graphene, graphene oxide and reduced graphene oxide **57**, 14543–14578. DOI: 10.1007/s10853-022-07514-z.

[15] McGilly, L. J. *et al.* Visualization of moiré superlattices **15**, 580–584. DOI: 10.1038/s41565-020-0708-3.

[16] Sen, A. K. Moiré patterns. *Computers & Graphics* **24**, 471–475 (2000). DOI: 10.1016/S0097-8493(00)00043-1.

[17] Du, L. *et al.* Moiré photonics and optoelectronics. *Science* **379**, eadg0014 (2023). DOI: 10.1126/science.adg0014.

[18] Carr, S., Fang, S. & Kaxiras, E. Electronic-structure methods for twisted moiré layers. *Nature Reviews Materials* **5**, 748–763 (2020). DOI: 10.1038/s41578-020-0214-0.

[19] Andrei, E. Y. & MacDonald, A. H. Graphene bilayers with a twist **19**, 1265–1275. DOI: 10.1038/s41563-020-00840-0.

[20] Wang, J., Mu, X., Wang, L. & Sun, M. Properties and applications of new superlattice: twisted bilayer graphene. *Materials Today Physics* **9**, 100099 (2019). DOI: 10.1016/j.mtphys.2019.100099.

[21] Cai, L. & Yu, G. Fabrication Strategies of Twisted Bilayer Graphenes and Their Unique Properties. *Advanced Materials* **33**, 2004974 (2021). DOI: 10.1002/adma.202004974.

[22] Carozo, V. *et al.* Resonance effects on the Raman spectra of graphene superlattices. *Physical Review B* **88**, 085401 (2013). DOI: 10.1103/PhysRevB.88.085401.

[23] Chen, H. *et al.* Atomically precise, custom-design origami graphene nanostructures. *Science* **365**, 1036–1040 (2019). DOI: 10.1126/science.aax7864.

[24] Wang, B. *et al.* Controlled Folding of Single Crystal Graphene. *Nano Letters* **17**, 1467–1473 (2017). DOI: 10.1021/acs.nanolett.6b04459.

[25] Zuo, J. M. & Spence, J. C. *Advanced Transmission Electron Microscopy* (Springer New York).

[26] Rochow, T. G. & Tucker, P. A. *Introduction to Microscopy by Means of Light, Electrons, X Rays, or Acoustics* (Springer US).

[27] Flegler, S. L. *Elektronenmikroskopie : Grundlagen - Methoden - Anwendungen* (Spektrum Akad. Verl., Heidelberg [u.a.], 1995).

[28] Michler, G. H. *Kompakte Einführung in die Elektronenmikroskopie*. essentials (Springer Fachmedien Wiesbaden, Wiesbaden, 2019).

[29] Bogner, A., Jouneau, P.-H., Thollet, G., Basset, D. & Gauthier, C. A history of scanning electron microscopy developments: Towards "wet-STEM" imaging. *Micron* **38**, 390–401 (2007). DOI: 10.1016/j.micron.2006.06.008.

[30] Brown, L. M. *Development of STEM*, chap. 3, 39–53 (John Wiley Sons, Ltd, 2011).

[31] Egerton, R. & Watanabe, M. Spatial resolution in transmission electron microscopy. *Micron* **160**, 103304 (2022). DOI: 10.1016/j.micron.2022.103304.

[32] Krivanek, O. *et al.* An electron microscope for the aberration-corrected era. *Ultramicroscopy* **108**, 179–195 (2008). DOI: 10.1016/j.ultramic.2007.07.010.

[33] Brydson, R. (ed.) *Aberration-Corrected Analytical Transmission Electron Microscopy* (Wiley), 1 edn.

[34] Williams, D. B. & Carter, C. B. *Transmission electron microscopy: a textbook for materials science* (Springer), 2nd ed edn.

[35] Egerton, R. *Electron Energy-Loss Spectroscopy in the Electron Microscope* (Springer US).

[36] Goodhew, P. J., Humphreys, F. J. & Beanland, R. *Electron microscopy and analysis* (Taylor & Francis), 3rd ed edn.

[37] Pennycook, S. J. & Nellist, P. D. (eds.) *Scanning Transmission Electron Microscopy* (Springer New York).

[38] Zhou, W. & Wang, Z. L. (eds.) *Scanning microscopy for nanotechnology: techniques and applications* (Springer).

[39] MacLaren, I., Macgregor, T. A., Allen, C. S. & Kirkland, A. I. Detectors—the ongoing revolution in scanning transmission electron microscopy and why this important to material characterization **8**, 110901. DOI: 10.1063/5.0026992.

[40] Scherzer, O. Über einige fehler von elektronenlinsen **101**, 593–603. DOI: 10.1007/BF01349606.

[41] University of Vienna. CANVAS (Nion UltraSTEM 100). https://physnano.univie.ac.at/equipment/canvas-nion-ultrastem-100/ [Accessed: 10.10.2023].

[42] Tanaka, N. *Electron Nano-Imaging* (Springer Japan).

[43] Ophus, C. Four-dimensional scanning transmission electron microscopy (4d-STEM): From scanning nanodiffraction to ptychography and beyond **25**, 563–582. DOI: 10.1017/S1431927619000497.

[44] Li, G., Zhang, H. & Han, Y. 4d-STEM ptychography for electron-beam-sensitive materials **8**, 1579–1588. DOI: 10.1021/acscentsci.2c01137.

[45] Yücelen, E., Lazić, I. & Bosch, E. G. T. Phase contrast scanning transmission electron microscopy imaging of light and heavy atoms at the limit of contrast and resolution. *Scientific Reports* **8**, 2676 (2018). DOI: 10.1038/s41598-018-20377-2.

[46] Caswell, T. *et al.* A high-speed area detector for novel imaging techniques in a scanning transmission electron microscope **109**, 304–311. DOI: 10.1016/j.ultramic.2008.11.023.

[47] Pennycook, T. J. *et al.* Efficient phase contrast imaging in STEM using a pixelated detector. part 1: Experimental demonstration at atomic resolution **151**, 160–167. DOI: 10.1016/j.ultramic.2014.09.013.

[48] Shibata, N. *et al.* Differential phase-contrast microscopy at atomic resolution **8**, 611–615. DOI: 10.1038/nphys2337.

[49] Mawson, T. *et al.* Factors limiting quantitative phase retrieval in atomic-resolution differential phase contrast scanning transmission electron microscopy using a segmented detector. *Ultramicroscopy* **233**, 113457 (2022). ArXiv:2108.08936 [cond-mat], DOI: 10.1016/j.ultramic.2021.113457.

[50] Hoppe, W. Beugung im inhomogenen primärstrahlwellenfeld. i. prinzip einer phasenmessung von elektronenbeugungsinterferenzen. *Acta Crystallographica Section A* **25**, 495–501 (1969). DOI: 10.1107/s0567739469001045.

[51] Guizar-Sicairos, M. & Thibault, P. Ptychography: A solution to the phase problem **74**, 42–48. DOI: 10.1063/PT.3.4835.

[52] Hofer, C. *et al.* Revealing the 3D structure of graphene defects. *2D Materials* **5**, 045029 (2018). DOI: 10.1088/2053-1583/aaded7.

[53] Graphenea, I. Easy transfer: Monolayer graphene on polymer film (2023). https://www.graphenea.com/collections/buy-graphene-films/products/easy-transfer-monolayer-graphene-on-polymer-film-1-cm-x-1-cm [Accessed: 11.09.2023].

[54] Ltd., S. Silson: Silicon nitrite tem grids (2023). https://www.silson.com/product/tem-windows-or-grids/ [Accessed: 11.09.2023].

[55] Mangler, C. *et al.* A materials scientist's CANVAS: A system for controlled alteration of nanomaterials in vacuum down to the atomic scale **28**, 2940–2942. DOI: 10.1017/S1431927622011023.

[56] Kofler, C. interferometric-4d-stem. https://github.com/kofcla/interferometric-4D-STEM.git (2023).

[57] Madsen, J. fourier-scale-calibration. https://github.com/jacobjma/fourier-scale-calibration (2022).

[58] Born, M. & Wolf, E. *Elements of the theory of interference and interferometers*, 286–411 (Cambridge University Press, 2019), 7 edn.

[59] Gross, R. & Marx, A. *Festkörperphysik*. De Gruyter Studium (De Gruyter, Berlin ; Boston, 2018), 3. auflage edn.

[60] Madsen, J. & Susi, T. The abtem code: transmission electron microscopy from first principles. *Open Research Europe* **1**, 13015 (2021). DOI: 10.12688/openreseurope.13015.1.

[61] Larsen, A. H. *et al.* The atomic simulation environment—a python library for working with atoms. *Journal of Physics: Condensed Matter* **29**, 273002 (2017).

[62] Bi, Z., Yuan, N. F. Q. & Fu, L. Designing flat bands by strain **100**, 035448. DOI: 10.1103/PhysRevB.100.035448.

[63] Barbosa, T. C. *et al.* Raman spectra of twisted bilayer graphene close to the magic angle **9**, 025007. DOI: 10.1088/2053-1583/ac4af9.

Appendix A

... but that was not the plan! A tale of broken equipment

The original plan for the thesis was quite optimistic. The main question has stayed the same - "What is the deal with the 3D structure of graphene?" But originally the idea was, to use the method of few tilt electron tomography, that was perfected by Christoph Hofer et al. in different papers [3, 52]. And like in their paper from 2022 [3], we wanted to combine it with ptychography to do state-of-the-art measurements. The paper from Zachman et al. [5], that was used in the end as the basis for the thesis was only a side-note I classified as – might be interesting as a comparison method if I have time.

So what happened to the original plan? The problems started already with the sample preparation. The idea was to use standard QUANTIFOIL™ gold TEM grids and transfer two layers of CVD grown graphene on top of each other – with the hope of finding some regions with small enough twist angles by diffraction measurements in the TITAN, our local TEM. The sample preparation was easy, however as soon as it was done, the TITAN decided to take a break and stop working for three months.

In these three months of downtime I researched different methods of getting information about the twist angle other than TEM, and ended up learning how to use the Raman spectrometer because of the change in the G and 2D bands of tBLG that indicates different twist angles (see e.g. [63]). I did not get the method working at all, but Wael Joudi mentioned in course of teaching me the spectrometer, that he regularly gets bilayer folds when he lasers his graphene monolayer samples on SiN grids.

So I ended up using his sample preparation method and it worked like a charm.

That was the solution to the first hurdle - however it came hand in hand with a number of new challenges, the most significant being mobile contamination that comes from the extreme cleanness of the samples. Fig. A.1 shows a sample area where a $\sim 8 \times 8$ nm region is completely covered by pinned down contamination after only a few seconds of imaging.

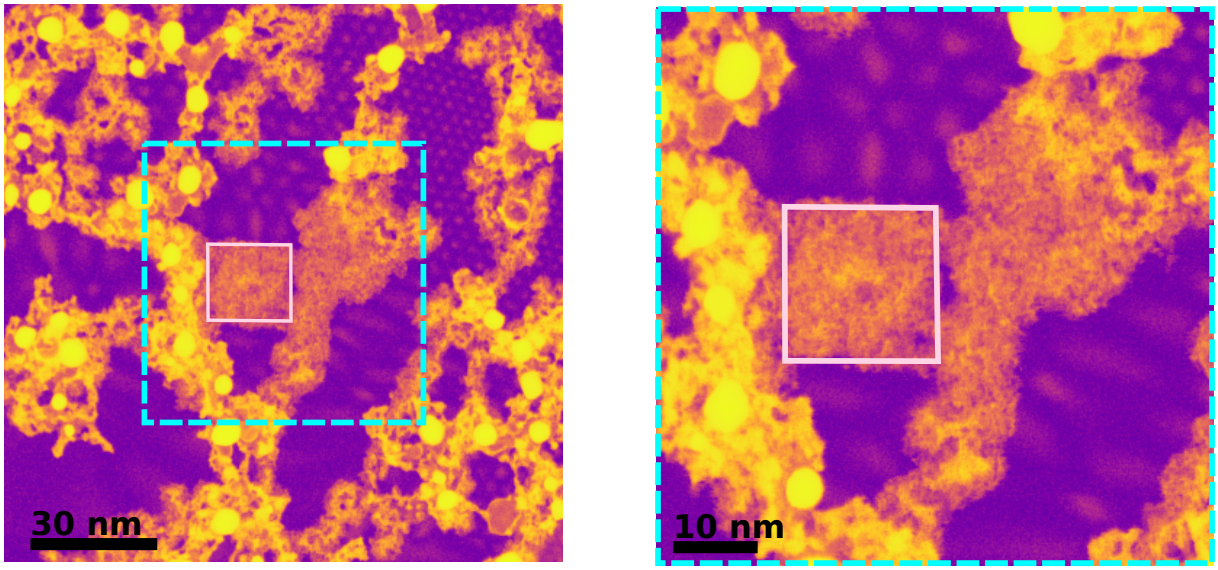

Figure A.1: Example STEM-MAADF images illustrating the effect of mobile contamination. The square of contamination marked in pink was pinned down by the electron beam by scanning over the region for less than a minute.

After laser treatment, the sample keeps clean for the first few hours, but at some point it starts contaminating, which makes imaging, and especially acquisition of 4D scan maps impossible.

Experimentally this means that the lasering has to be followed by immediate imaging, which makes the use of tilt tomography impossible as the samples have to be placed in a special tilt cartridges for these experiments and our current setup does not offer an option for in-situ lasering in the microscope column.

That this method was off the table was just as well, because on the second front of our efforts, the installation of our new direct electron detectors, the Timepix, different battles were fought and lost in the meantime and progress was slow.

It took us multiple tries to get the Timepix installed in our column, each of these vacuum construction sessions connected to a risk for the microscope. We managed in the end, not before introducing an aperture fault that made imaging impossible for a while. The software syncing was the next problem. Even with the detector chip in its place, getting useful data is no piece of

cake. The relentless work of Clemens Mangler and Alissa Freilinger paid off in the end and now nothing stands in the way of recording data with the new setup. For this thesis however, there was just not enough time to integrate the recently functional detector in the experiments.

So I took the original plan for the experiments and cut off only a tiny sliver of what we planned to do and concentrated on that: Interferometric 4D-STEM.

The samples were at that point already nicely characterised, with mapped regions of small twist angles perfect for comparison with the relaxed structures calculated by Florian Libisch at the TU Vienna. However, when the time had come to record actual data, a height change of the stage of the microscope made it impossible to use these samples and new ones had to be prepared and lasered upside down.

So that was the path of broken equipment that has lead from the elaborate original plan to the fragment of barely useable data presented in this thesis.